NTNU

Norwegian University of
Science and Technology

Computational Study of Hydraulic Accumulators

Espen Charles Brekka Hiis

Subsea Technology
Submission date: June 2018
Supervisor: Olav Egeland, MTP
Co-supervisor: Boris Balakin, HVL
Gleb Pisarev, OneSubsea

Norwegian University of Science and Technology
Department of Mechanical and Industrial Engineering

Abstract

The scope of this project is to make a CFD model to be used for getting a better understanding of accumulator discharge. To be able to establish the models credibility is there a need for validation of the models developed. First a model of one accumulator is to be validated by use of an experimental project as well as an analytical approach. This model is then to be adapted to a system of two accumulators in series to be studied and validated by a theoretical equation developed.

The literature review reveal that the study of accumulator discharge for applications for the oil industry is not a area were many articles is presented, which makes the scope of this thesis more interesting.

The first case studied is a single bladder-type accumulator, which is discharged through three different outlet areas and has an internal volume of 4 l, with a pre-charge pressure of 2 bar. The physical model developed is validated by experimental data, and a theoretical approach to establish the models credibility. The average discrepancies obtained from the results was below 12.56% for all cases modeled. These results shows a high level of agreement to the various validation points, which leads to significant credibility of the physical model developed. This model is then to be adapted to the following cases in this study.

The second case studies discharge of a set of two 40 l accumulators placed in series with different pre-charge pressures, but equal charge pressure. The case studies the effect of changing the ambient temperature, outlet area of the discharge nozzle, and different outlet pressures (backpressure). The obtained results shows that the effect of various ambient temperature will not have a significant impact on the discharge pattern, but by changing the restrictions in the outlet nozzle the profiles obtained showed great deviation from the base case computation. Where the variation of outlet area of the nozzle had a bigger impact on the discharge than by changing the backpressure in the system. An observation from this case shows that the pressure drop in the accumulator with the lowest pre-charge had a rapid pressure drop in the first part of the discharge cycle. This pressure drop is caused by the flow pattern out of the given accumulator.

The last case studied is a similar case as the one above, but with accumulator volumes of 10 l each. In this case the effect of changing the pre-charge order, as well as the backpressure was studied. The results obtained from this study shows that changing the pre-charge order will provide a more constant pressure delivery without a rapid pressure drop in the system. This will result in a more stable and predictable flow out of the hydraulic system studied. Even when changing the restrictions in the outlet nozzle, the results shows a more stable flow out of the system, with similar pressure profiles.

Sammendrag

Omfanget av dette prosjektet er å lage en CFD-modell som skal brukes til å få bedre forståelse av akkumulatorutladning. For å kunne etablere modellens troverdighet er det behov for validering av modellene som er utviklet. Først skal en modell av en akkumulator bli validert ved bruk av et eksperimentelt prosjekt, samt en analytisk tilnærming. Denne modellen skal da tilpasses et system med to akkumulatorer i serie for å bli studert og validert av en teoretisk ligning utviklet.

Litteraturvurderingen viser at forskning av discharge av akkumulatorer til oljeindustrien ikke er et område hvor mange artikler er presentert, noe som gjør omfanget av denne avhandlingen mer interessant.

Det første tilfellet som studeres, er en blæreakkumulator som utlades gjennom tre forskjellige utløpsområder og har et internt volum på 4 l, med et forladningstrykk på 2 bar. Den utviklede fysiske modellen er validert av eksperimentelle data og en teoretisk tilnærming for å etablere modellens troverdighet. Gjennomsnittlig avvik fra resultatene var under 12,56% for alle tilfeller modellert. Disse resultatene viser høy grad av nøyaktighet til de ulike valideringspunktene, noe som fører til betydelig troverdighet i den utviklede fysiske modellen. Denne modellen skal videre tilpasses de følgende tilfeller i dette studiet.

Den andre casestudien tar for seg et sett med to 40 l akkumulatorer plassert i serie med forskjellige forladetrykk, men likt ladetrykk. Casen undersøker effekten av å endre omgivelsestemperaturen, utløpsareal til utløpsdysen og forskjellige utløpstrykk (mottrykk). De oppnådde resultatene viser at effekten av forskjellige omgivelsestemperaturer ikke vil ha vesentlig innvirkning på utladningsmønsteret, men ved å endre restriksjonene i utløpsdysen viste profilene store avvik fra grunnmodellen. Hvor variasjonen av dysens utløpsområde hadde større innvirkning på utladningen enn ved å endre mottrykket i systemet. En observasjon fra dette tilfellet viser at trykkfallet i akkumulatoren med den laveste forladningen hadde et raskt trykkfall i den første delen av utladningsyklusen. Dette trykkfallet er forårsaket av strømningsmønsteret ut av den oppgitte akkumulatoren.

Det siste tilfelle som studeres er et lignende tilfelle som det ovenfor, men med akkumulatorvolume på 10 l hver. I dette tilfellet ble effekten av å endre forladningsrekkefølgen samt mottrykket undersøkt. Resultatene fra denne undersøkelsen viser at endring av forladningsrekkefølgen vil gi en mer konstant trykklevering uten et raskt trykkfall i systemet. Dette vil resultere i en mer stabil og forutsigbar strømning ut av det hydrauliske systemet som studeres. Selv når du endrer restriksjonene i utløpsdysen, viser resultatene en mer stabil flyt ut av systemet med lignende trykkprofiler.

Preface

This thesis is submitted as a final assignment for obtaining the degree of Master of Science in Subsea Technology, Operation and Maintenance at the Norwegian University of Science and Technology. The work is conducted at the department of Mechanical and Industrial Engineering, at the faculty of Engineering. The project is carried out over 20 weeks, and is awarded with 30 credits.

I would like to express my gratitude to my supervisor Boris V. Balakin and the Department of Mechanical and Marine Engineering at Western Norway University of Applied Sciences for the support throughout this study. I would also like to thank Gleb Pisarev and OneSubsea Processing AS for supporting me with information when needed, and giving me the opportunity to carry out my Master thesis under their supervision. Last but not least I would like to thank Marcus A. Stenhjem for providing me with experimental data.

Bergen, 11. June 2018

Espen Ch. Hiis

Table of Contents

List of Tables

List of Figures

Abbreviations

ρ	Density [kg/m^3]
u	Velocity component in X-direction [m/s]
v	Velocity component in Y-direction [m/s]
w	Velocity component in Z-direction [m/s]
F	Force [N]
m	Mass [kg]
a	Acceleration [m/s^2]
$\mathbf{V}$	Velocity vector notation [m/s]
τ	Shear stress [N/A]
γ	adiabatic index
P	Pressure [Pa]
λ	Thermal Conductivity [W/m K]
ϕ	Volume fraction
μ	Viscosity [Pa s]
f_x	Body forces in X-direction [N]
f_c	Capillary forces [N]
e	Internal energy
Re	Reynolds number
D_p	Pipe diameter [m]
T	Temperature [K]
Γ	Turbulent time scale
f_μ	Dampening function
k	Kinetic energy
ϵ	Dissipation rate
κ	von Karman's constant
f	Friction coefficient
V	Volume [m^3]
$\dot{q}$	Heat flux [W/m^2]
ψ	Discharge coefficient
R	Gas constant [8.314 kgm^2/molKs^2]
A	Area [m^2]
t	Time [s]
Q	Volume flow [m^3/s]
Ω	Total heat [W]
h	Convective heat transfer coefficient [W/m^{2}K]

Chapter 1

Introduction

The scope of this master thesis is to design and model three different cases of accumulator discharge. Case one is discharge of a bladder-type accumulator used in an experimental project executed parallel to this study, the second case is a set of two piston accumulators placed in series based on a industrial system, and treated as a generalized case. The third case is similar to the second, but the geometries of the accumulators is equal to system obtained from a cooperative company. Validation of the program is to be carried out for cases one and three to obtain credibility of the model. The 3D numerical program STAR-CCM+ will be used to calculate discharge of the models. Further in this chapter, information about the system and background for this thesis will be described.

1.1 Hydraulic accumulator

Hydraulic accumulators is modified pressure vessels used to store energy by means of pressurized hydraulic fluid. Since this fluid is in-compressible there is a need for an external force to pressurize the fluid, there are multiple ways of executing this force, shown in figure 1.1. Further in this thesis the gas-charged bladder- and piston-type accumulator will be taken under consideration.

The bladder-type accumulator consists of a accumulator body with a elastic bladder inside that separates the gas and fluid. While the piston-type accumulator is composed of a cylindrical pressure vessel with a floating piston inside that separates the gas from the hydraulic fluid. Usually nitrogen is used to pressurize the hydraulic fluid because of its ability to stay stable under high pressure and temperature, and it will not chemically interact with the hydraulic fluids if they are exposed to one another. To obtain the pressure in the accumulator it is important that the gas and fluid do not mix. If there is a leak from the gas side to the liquid side, the accumulator will lose some of its power and it will no longer be as reliable. The components that prevent this from happening are seals between the piston and the accumulator housing. It is important that the seals are as dense as possible without influencing piston-casing friction negatively.

An important factor when it comes to the piston accumulator is the friction between the piston and the housing. There are different types of factors affecting the overall friction.

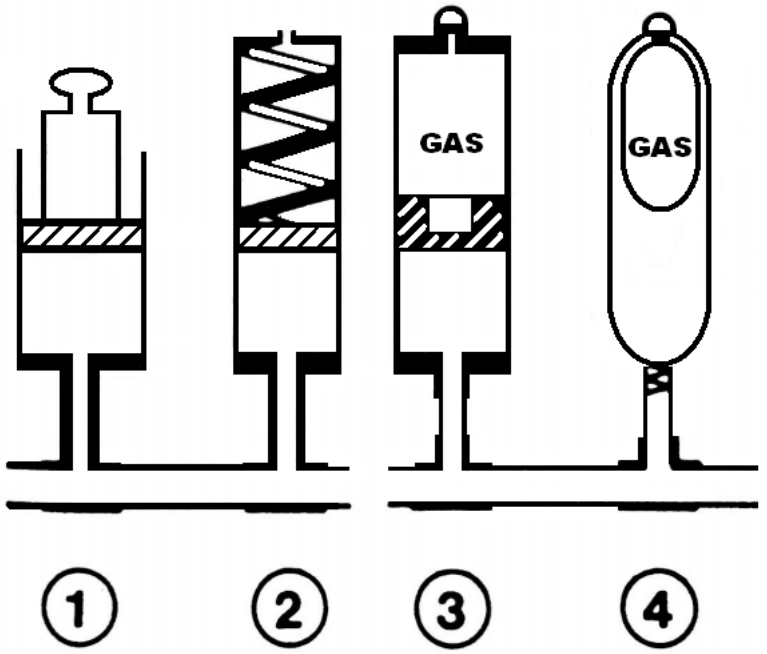

Figure 1.1: Illustrative figure of weight (1), spring (2) and gas charged (3,4) accumulators (Kjolle, 1989).

Friction force is a function of relative velocity of the piston and pressure, and is assumed to be the sum of Stribeck, Coulomb and viscous components. The Coulomb friction force is dependent on the preload force, caused by the seal squeeze during assembly of the accumulator, and is proportional to pressure. The sum of Coulomb and Stribeck friction forces at zero velocity is often referred to as the breakaway friction force, meaning the absolute value of force needed to make the piston move (Haq, 2010).

1.2 Experimental and theoretical

The experimental project was carried out by Stenhjem (2018), parallel to this study. The part of interest is discharge of the bladder accumulator through three different valve openings, in room temperature of $20°C$, the valve openings is shown in Table 4.1. The experimental project is described in Stenhjem (2018), and consists of a 4 l bladder-type accumulator and the outlet area is regulated by a gate valve. The gas used for precharge of the accumulator was pressurized air, and the fluid used was a mixture of water and glycol. This project together with a analytical approach obtained from Hiis and Stenhjem (2017) is to be used for validation of the model made in STAR-CCM+. The model developed,

was then the base line for the model of use in the case of solving problems accruing with in a barrier fluid hydraulic power unit.

The theoretical equation of accumulator discharge through a nozzle is derived in Hiis and Stenhjem (2017), the equation for pressure with respect to time is shown in Eq. 1.1 below.

$$P(t) = \left(\frac{1}{\frac{\beta t(\gamma+2)}{2\alpha} + P_o^{-\frac{\gamma+2}{2\gamma}}} \right)^{\frac{2\gamma}{\gamma+2}} \tag{1.1}$$

Where P_0 is the initial pressure of the gas, γ is the adiabatic index, α and β are constants, and t is time, the derivation of this equation is shown in detail in Hiis and Stenhjem (2017).

1.3 Industrial case

The system of interest is a barrier fluid system for a subsea multiphase pump used for boosting oil and gas production wells, and consists of a hydraulic power unit with a set of accumulators and valves. In this section the system is described.

1.3.1 Hydraulic power unit (HPU)

Hydraulic power unit is a unit consisting of hydraulic pumps, reservoirs, pipes and hydraulic accumulators. The main purpose of the HPU is to deliver pressurized hydraulic fluid to various users on the seafloor or platform. In the case described in this thesis the hydraulic fluid is used as barrier fluid for a subsea multiphase pump. The HPU is located topside and dry on the platform, and the hydraulic fluid is delivered through an umbilical to the seabed facilities.

1.3.2 Barrier fluid

The barrier fluid system contributes to lubricate and cool the motor and pump bearings under normal operation, but it also allows keeping an overpressure in the motor casing to avoid production fluids and water to penetrate into the electrical parts of the motor. Due to this overpressure, there is a leakage across the mechanical seal. To avoid a continuous refill of the barrier fluid, is the sealing designed to keep the leakage to a minimum (Thibaut et al., 2010). The barrier fluid used in this application is *Shell Morlina S2 BL 5*, which is a low viscosity, solvent refined mineral oil blended with zinc free additives, designed for high speed spindles for machine tools. The physical characteristics was provided by the cooperative company, and is presented in table 1.1 below.

Desity	869 kg/m^3
Kinematic Viscosity	5 mm^2/s
Specific Heat	1670 J/kg K
Thermal Conductivity	0.152 W/m K

Table 1.1: Properties of barrier fluid

1.4 Objective

To be able to ensure the over-pressure on the mechanical sealing for the multiphase pump, is there a design loss of hydraulic fluid over this seal and into the production flow. Which means that the accumulator will be charged and discharged in a cyclic manner.

The operator notice some irregularities when discharging the pressure inside the accumulator. In the first few minutes of operation after charge pressure is reached, is there a rapid pressure drop before the systems stabilizes. This drop of pressure is not always understood, it is desirable for the operator to identify this pressure drop, and get a better understanding of the discharge cycle.

The scope of this project is to make a CFD model to be used for getting a better understanding of accumulator discharge, in that case the model has to be validated for establishing its credibility. First a model of one accumulator is to be validated by use of an experimental project as well as a analytical approach. This model is then to be adapted to a systems of two accumulators to be studied and validated by a theoretical equation developed.

Chapter 2

Literature Review

Hydraulic accumulators, where fluid is pressurized inside a cylinder was first invented by William Armstrong to be used during on- and offloading of ships in the mid 1800s. In this device a vertically closed cylinder with a ram inside were loaded by dead weight ballast, with energy able to be stored by upward movement of the ram, and restored on the decent (Gibson and Pierce, 2010). The first gas-charged accumulator was invented by Jean (1943), who filed the patent for the first bladder type accumulator, to be used in the aircraft industry. The invention consists of rigid housing with an elastic bladder inside. The bladder was to be pre-charged with a suitable gas, while the other chamber was to be filled with an hydraulic fluid to compress the gas and increasing the pressure, which results in an energy storage. In later years, to be able to reach different application demands the piston type accumulator was designed. The piston type accumulator was invented by Ashton (1948), who filed a patent of a accumulator to improve its ability to absorb shock in the hydraulic system and accumulating a reserve of the liquid so that the pressure in the system is maintained more closely in the predetermined pressure limits. The design is similar to the bladder type, but the physical divider is a floating piston instead of a rubber bladder.

Accumulators is a widely used application in everything from wind turbines to safety devices in nuclear power plants, and is studied in depth in several of these areas.

Accumulators is frequently used as pitch control of the blades on a wind turbine. The accumulator is used due to its ability to provide real time control and because of its low response time in high risk situations as emergency stops, or when extra power is needed to change the pitch angle in the blades while the wind turbine is operating. Due to the importance of the reliability of this kind of system, Irizar (2015) studies the charge and discharge cycle of a piston accumulator used in a pitch control system in a thermal perspective by use of experiments and computational fluid dynamics.

The result obtained from Irizar (2015) shows that the pressure evolution from the CFD simulation has a good level of agreement with experimental reference, which provides a solid validation point for the model. The study conducted by Irizar (2015) answers the thermodynamic process of an accumulator charge and discharge cycle, but is not focusing on the pressure profiles while discharging as done in the the study conducted in this report.

Mitsubishi Heavy Industries (2011) studies a scaled Advanced Accumulator (ACC), which is a safety feature. This modified type of accumulators is used in nuclear power

plants to supply coolant to the primary circulation loop in case of the potential meltdown emergency. It is important to have a great understanding of how the flow acts when the accumulator is discharged, Mitsubishi Heavy Industries (2011) studies the flow characteristics to better understand, and verify the performance of a half scaled, full height accumulator model in a computational fluid dynamics perspective. The results obtained in this study shows a good similarity for the flow structure, and when comparing the half scaled model to a full scale model the results shows that the scaling effect is small compared to the experimental uncertainties. The results obtained from Mitsubishi Heavy Industries (2011) is very promising, but the topic does not touch upon the cases studied in this thesis.

Due to the fact that the model developed in this thesis is mainly focused on the pressure profile and discharging pattern, the articles presented above has some interesting results, but the topics in these studies does not answer the study presented in this thesis. The discharge of accumulators used in applications for the oil industry is not a area were many articles is presented, which makes the scope of this thesis more interesting.

Chapter 3

Basic Theory

3.1 Basic equations

The governing equations of fluid dynamics is the base of CFD, the most important equations is continuity, momentum and energy equations. In this section the three equations is described and stated.

3.1.1 Continuity equation

In fluid mechanics, the equation of continuity states that the amount of mass entering the system combined with accumulated mass in the system is equal to the mass leaving this system. The derivation of this equation follows the physical principle, conservation of mass (Anderson, 1995).

If an infinitesimally small box-element fixed in space is considered, with fluid moving through, and sides dx, dy, dz, as shown in Figure 3.1. The mass flow ($\dot{m}$) entering this element is equal to the density (ρ), velocity in the given direction (u,v,w), and the cross-section of the area where fluid enters. When considering the left and right face of the element which are perpendicular to the x axis. Mass flow through the left side is $(\rho u)dy\ dz$. The mass flow contribution from y and z direction to the x direction in the element can be expressed as $(\partial(\rho v)/\partial x)dx\ dy\ dz$. Flow out of the right face is expressed as $\{\rho u + [\partial(\rho u)/\partial x]\, dx\}dy\ dz$. If the outflow of mass is a positive number, the net outflow in x,y and z direction can be expressed as (Anderson, 1995):

Net outflow in x direction:

$$\left[\rho u + \frac{\partial(\rho u)}{\partial x}dx\right]dy\ dz - (\rho u)\ dy\ dz = \frac{(\partial u)}{\partial x}dx\ dy\ dz$$

Net outflow in y direction:

$$\left[\rho v + \frac{\partial(\rho v)}{\partial y}dy\right]dx\ dz - (\rho v)\ dx\ dz = \frac{(\partial v)}{\partial y}dx\ dy\ dz$$

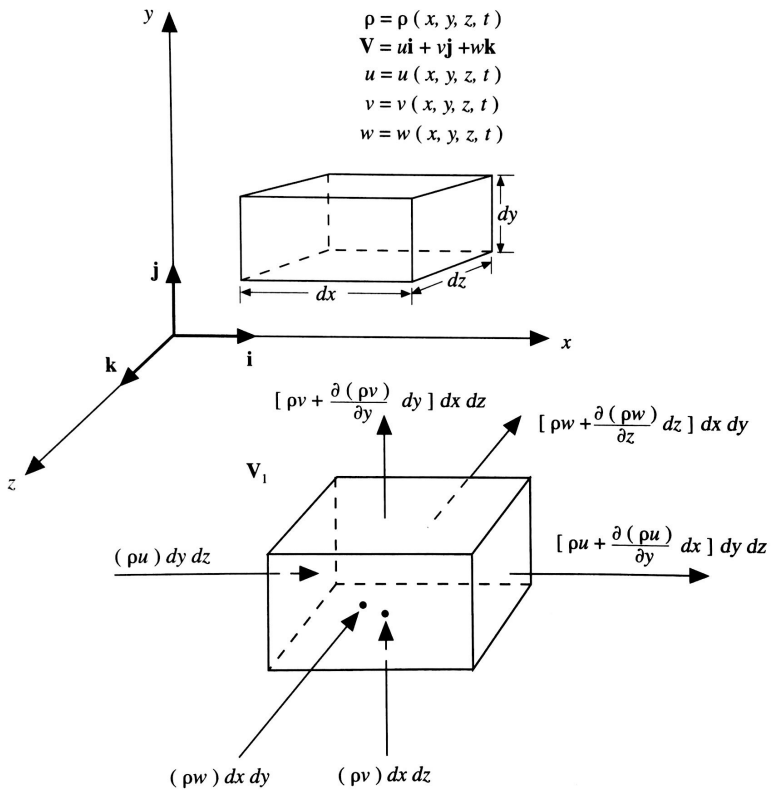

Figure 3.1: Model of infinitesimally smal element fixed in space and a diagram of mass flux through the various faces of the element (Anderson, 1995).

Net outflow in z direction:

$$\left[\rho w + \frac{\partial(\rho w)}{\partial z} dz\right] dx\ dy - (\rho w)\ dx\ dy = \frac{(\partial w)}{\partial z} dx\ dy\ dz$$

The total net flow out of the element is given by

$$Net\ mass\ flow\ = \left[\frac{(\partial u)}{\partial x} + \frac{(\partial v)}{\partial y} + \frac{(\partial w)}{\partial z}\right] dx\ dy\ dz \tag{3.1}$$

The total mass of fluid inside this element of a given time is $\rho\ (dx\ dy\ dz)$, so the time rate of mass increasing in the element is given by

$$Time\ rate\ of\ mass\ increase\ = \frac{\partial \rho}{\partial t}(dx\ dy\ dz) \tag{3.2}$$

When the physical principle conversation of mass is applied, will the net mass flow out of the element be equal to the decrease of mass inside. By putting Equation 3.1 and 3.2 together, the continuity equation will read:

$$\frac{\partial \rho}{\partial t} + \left[\frac{(\partial u)}{\partial x} + \frac{(\partial v)}{\partial y} + \frac{(\partial w)}{\partial z} \right] = 0 \tag{3.3}$$

If the term inside the brackets is expressed as $\nabla \cdot (\rho \mathbf{V})$, then Eq. 3.3 can be simplified to

$$\frac{\partial \rho}{\partial t} + \nabla \cdot (\rho \mathbf{V}) = 0 \tag{3.4}$$

Equation 3.3 is the partial differential equation form of the continuity equation, on the basis that the element fixed i space, it is by definition called the conservation form (Anderson, 1995).

3.1.2 Momentum equation

To be able to derive the momentum equation the fundamental physical principle of Newton's second law is applied:

$$\vec{F} = m\vec{a} \tag{3.5}$$

Newton's second law, shown in Equation 3.5 says, when applied to a fluid element as shown in Figure 3.2, that the net force on the fluid element equals the mass times the acceleration of the element. This is a vector relation, and can be split into three scalar relations along x, y, and z-axis (Anderson, 1995).

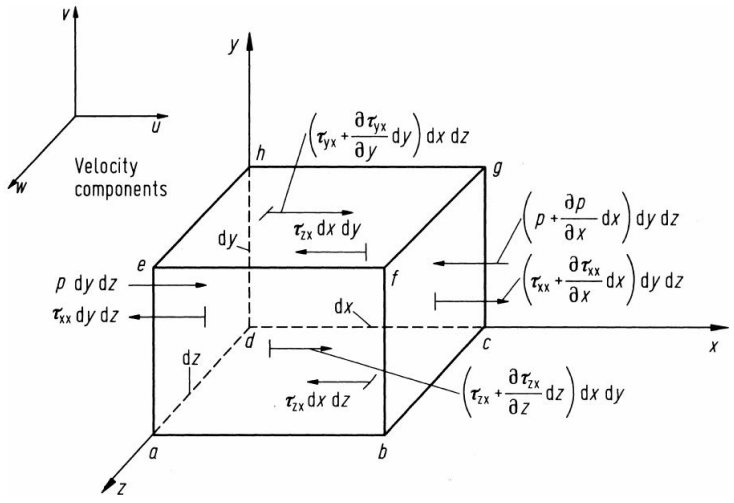

Figure 3.2: Infinitesimally small, moving fluid element. Only the forces in the x direction are shown (Anderson, 1995).

In the given direction there are two different sources of force acting on the element, body, and surface forces. Body forces are forces that act directly on the mass of the fluid

element, magnetic, electric and gravitational forces are some examples of these forces. The surface force are forces acting on the surface of the element, this is due to the distribution of pressure on the surface caused by the fluid surrounding the element, as well as friction forces caused by the share stress and normal stress action on the surface. The conversation form of the momentum equation in x-direction is presented in Equation 3.6, which is known as the Navier-Stokes equation (Anderson, 1995).

$$\frac{\partial(\rho u)}{\partial t} + \nabla \cdot (\rho u \mathbf{V}) = -\frac{\partial p}{\partial x} + \frac{\partial \tau_{xx}}{\partial x} + \frac{\partial \tau_{yx}}{\partial y} + \frac{\partial \tau_{zx}}{\partial z} + \rho f_x \tag{3.6}$$

Where $\nabla \cdot (\rho u \mathbf{V})$ comes from the rate of change of velocity in the x-direction, τ_{xx} is the normal stress, τ_{yx}, τ_{zx} is the share stress, and ρf_x represents the body force action on the fluid element in the x-direction (Anderson, 1995).

3.1.3 Energy equation

To derive the energy equation there is used an infinitesimally small fluid element moving with the flow, as well as the physical principle that energy is conserved, which is the first law of thermodynamics. When applied to the flow model of a fluid element moving with the flow, the first law states:

$$A = B + C \tag{3.7}$$

where A is the rate of change of energy inside the fluid element, B is the net flux of heat into the element, and C is the work done on the element due to body and surface forces. The full derivation of the energy equation can be found in Anderson (1995). Energy fluxes combined with the fluid element is shown in Figure 3.3, the full energy equation is shown in Equation 3.8 (Anderson, 1995).

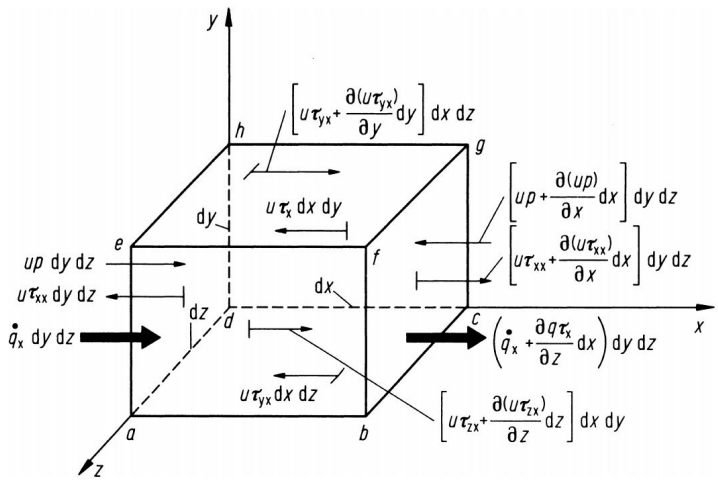

Figure 3.3: Energy fluxes associated with an infinitesimally small, moving fluid element for x direction (Anderson, 1995).

$$
\begin{aligned}
&\frac{\partial}{\partial t}\left[\rho\left(E\right)\right]\cdot\left[\rho\left(E\right)\mathbf{V}\right] \\
&=\rho\dot{q}+\frac{\partial}{\partial x}\left(\lambda\frac{\partial T}{\partial x}\right)+\frac{\partial}{\partial y}\left(\lambda\frac{\partial T}{\partial y}\right) \\
&+\frac{\partial}{\partial z}\left(\lambda\frac{\partial T}{\partial z}\right)-\frac{\partial(up)}{\partial x}-\frac{\partial(vp)}{\partial y}-\frac{\partial(wp)}{\partial z}+\frac{\partial(u\tau_{xx})}{\partial x} \\
&+\frac{\partial(u\tau_{yx})}{\partial y}+\frac{\partial(u\tau_{zx})}{\partial z}+\frac{\partial(v\tau_{xy})}{\partial x}+\frac{\partial(v\tau_{yy})}{\partial y}+\frac{\partial(v\tau_{zy})}{\partial z} \\
&+\frac{\partial(w\tau_{xz})}{\partial x}+\frac{\partial(w\tau_{yz})}{\partial y}+\frac{\partial(w\tau_{zz})}{\partial z}+\rho\mathbf{f}\cdot\mathbf{V}
\end{aligned}
\tag{3.8}
$$

Where the term $E=(e+V^2/2)$ represents the total energy where e is the contribution from internal energy, and $V^2/2$ is the kinetic energy due to translational motion of the fluid element, $\dot{q}$ is the heat transferred by thermal conduction, **f** is the total body force acting on the fluid element, and λ is the thermal conductivity (Anderson, 1995).

3.2 Piston friction

No matter where there is contact between two solids, will there be a frictional force between them. In a hydraulic cylinder where the piston is moving will the problem of friction also arise. As mentioned in section 1.1 the only contact between the accumulator housing and the piston is the piston seals. To be able to minimize the friction force, the contact area between the two moving bodies needs to be as small as possible.

The friction force between the piston seal and accumulator body is modeled as a function of pressure and relative velocity of the piston, and is assumed to be the sum of Stribeck, Coulomb and viscous components. The Coulomb friction force consists of the preload force caused by seal squeeze during assembly and the force proportional to pressure, and is independent of piston velocity, which is the electrostatic force. The viscous friction component is assumed to be proportional to the velocity, where this contribution will increase with the speed of the piston. At low velocities the friction phenomena of Stribeck will arise, this friction force originates from where lubrication is lacking, and is modeled as exponential decay from breakaway friction force close to zero velocity to the coulomb component (Armstrong-Hélouvry et al., 1994). The sum of these friction forces is shown in Figure3.4.

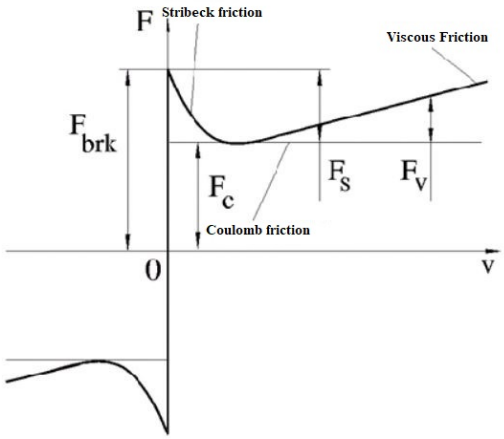

Figure 3.4: Total friction force (Mathworks, 2017).

From Figure 3.4 the representation of the contribution of the different frictions is shown, where F_{brk} is the breakaway/stick friction, F_C is the coulomb friction, F_S is the stribeck friction, and F_V is the viscous friction. The total friction force can be approximated with Equation 3.9 below.

$$F = \sqrt{2e}(F_{brk} - F_C) \cdot e^{-\left(\frac{v}{v_{St}}\right)^2} \cdot \frac{v}{v_{St}} + F_C \cdot tanh\left(\frac{v}{v_{Coul}}\right) + fv \qquad (3.9)$$

Where F is the total friction force, v is the relative velocity of the piston, v_{St} is the Stribeck velocity, v_{Coul} is the Coulumb velocity, and f is the viscous friction coefficient (Mathworks, 2017).

3.3 Computational fluid dynamics

Computational fluid dynamics (CFD) is the use of applied mathematics, physics and computational software to analyze fluid flow. Numerical methods is used to solve the Navier-Stokes equations in a CFD software.

3.3.1 Discretization

Discretization can be defined as a process where a closed-formed mathematical expression, like a function, differential or integral equation that involves functions, considered having an infinite continuum of values throughout some domain. These functions are approximated by an analogous expression that obtains values only on a limited number of discrete points or volumes in the given domain. A partial differential solution solved numerically can only give an answer at discrete point in the given domain, these points are

called grid points. Representation of a discrete grid in the xy plane is shown in Figure 3.5 (Anderson, 1995).

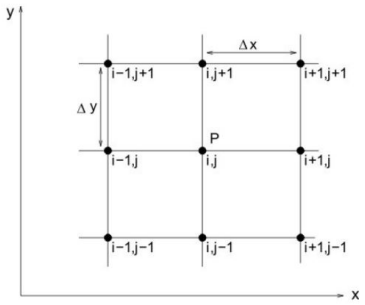

Figure 3.5: Discrete grid points (Anderson, 1995).

The grid points can be identified by an index i and j which evolves in the x and y direction respectively, and the distance between points in x direction is Δx and distance in y direction is Δy. Discretization is to transform a partial differential equation to a set of equations where the variables in one cell are a function of the variables of the neighboring cell, which will define a solution for the given domain (Anderson, 1995).

3.3.2 Mesh

Mesh is a discretized representation of the computational domain, which the physics is solved by numerical methods. The arrangement of these discrete points throughout the flow field is called a grid, the way such a grid is determined is called grid generation. The grids can be classified by different characteristics like structure, shape and orthogonality.

Structured and unstructured grids are the two different fundamental classes when it comes to grid generation. The difference of these classes is the way in which the grid points are locally organized. A structured mesh is independent of the local organization and the from of the grid cells, and is defined by a general rule, while an unstructured mesh is defined if the neighboring grid nodes varies from point to point. As a result, in the structured case the connectivity of the grid is implicitly taken into account, while the connectivity of unstructured grids must be explicitly described by an appropriate data structure (Liseikin, 2010). A representation of structured and unstructured grid is shown in Figure3.6.

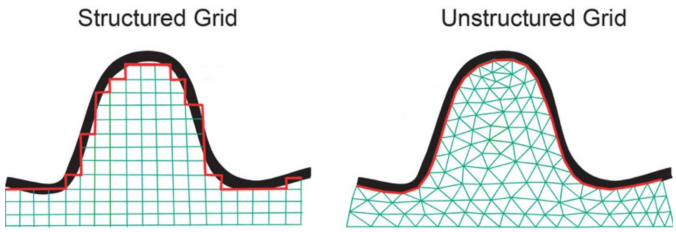

Figure 3.6: Representation of structured grid (left) and unstructured grid (right) (NOAA, 2018).

As can be seen from Figure 3.6 the advantages of unstructured grid is its ability to fit the geometry, the disadvantage is that the solver requires a more complex code to identify the neighboring cells.

When creating a 3D grid with varying geometry there is different cell shapes to be used for meshing, the most common types is trimmed, polyhedral and tetrahedral. Of these three cell types there is the tetrahedral mesh that provides the most efficient solution and uses the least amount of computational power for a given number of cells. However, the use of tetrahedral meshing uses approximately five to eight times more cells to achieve the same accuracy as polyhedral and trimmed type. The polyhedral meshes provide a balanced solution for complex mesh generation problems, and is relatively easy to fit and efficient to build. The trimmed cell mesh is a robust and efficient method of producing grids for both simple and complex mesh generation, and is constructed by hexahedral cells (Siemens, 2017).

The orthogonality of the grid is determined by the angle between crossing grid lines. If this angle is 90 degrees, the grid can be considered orthogonal. If the angle differs from 90 degrees, the grid can be considered non-orthogonal. A orthogonal grid will often lead to more rapid convergence, and in some cases result in better accuracy (Olsen, 2007).

Other characteristic used to define the quality of the grid is volume change, the volume change describes the ratio of volume of a cell to that of its largest neighbor. A value of unity indicates that the cell has volume equal to or higher than its neighbors. If the volume change is less than 0.01, it can be considered as a bad cell, and a large jump in volume from one cell to another can cause potential inaccuracies and instability in the solvers. A good quality mesh is very important for achieving an accurate and efficient solution (Siemens, 2017).

3.3.3 Volume Of Fluid (VOF)

In each cell of a mesh it is customary to use only one value for each dependent variable defining the fluid state. The volume of fluid method defines a function, that if the value of this function is equal to unity, will correspond to a cell completely occupied by fluid, while a value of zero indicates that the cell contains no fluid. Cells with values between unity and zero must than contain a free surface (Hirt and Nichols, 1981). The model, constructed in STAR-CCM+, assumes that the flow of both phases can be described by a set of Navier-Stokes equations for the viscous flow. The continuity equation fore each

phase is described by Equation 3.10.

$$\frac{\partial(\phi_j \rho_j)}{\partial t} + \nabla(\phi_j \rho_j \mathbf{V}) = 0 \tag{3.10}$$

Where ϕ represents the volume fraction for each phase, $j = l$ for liquid and $j = g$ for gas, where $\phi_l + \phi_g = 1$, ρ is the phase density and $\mathbf{V}$ is the velocity, assumed to be equal for each phase in the computational cell.

The two-phase homogeneous mixture with phases at volume fractions ϕ_g and ϕ_l is assumed to exist in the computational cell in a way where the molecular properties of the mixture is given by Equation 3.11 below (Balakin et al., 2017).

$$\begin{aligned} \rho_m &= \rho_l \phi_l + \rho_g \phi_g \\ \mu_m &= \mu_l \phi_l + \mu_g \phi_g \end{aligned} \tag{3.11}$$

For the mixture, the conservation of momentum is shown in Equation 3.12

$$\rho_m \frac{\partial \vec{u}}{\partial t} + \rho_m \vec{u} \nabla \mathbf{V} = -\nabla p + (\mu_m + \mu_m^t)\Delta \vec{u} + \rho_m \vec{g} + \vec{f_c} \tag{3.12}$$

Where p is pressure, μ_m and μ_m^t is molecular and turbulent viscosity respectively, and $\vec{f_c}$ is the capillary force calculate by Eq 3.13.

$$\vec{f_c} = \nabla \cdot \left(\frac{\nabla \phi_l}{|\nabla \phi_l|} \right) \nabla \phi_l \sigma \tag{3.13}$$

Where σ is the surface tension (Balakin et al., 2017).

The conservation of energy is shown in Equation 3.14

$$\frac{\partial(\rho E)}{\partial t} + \nabla \cdot (v(\rho E + p)) = \nabla \cdot (\lambda \nabla T) + \Omega \tag{3.14}$$

Where E is the total energy in the system, which is the sum of internal and kinetic energy, and Ω is the total heat in the system (Wang and Zhuan, 2009).

3.3.4 Turbulent flow

In most practical situations where fluid flows through a pipe the flow will act turbulent. Turbulent flow is a flow regime where the fluid acts unpredictable and contains vortices, wakes and eddies. To be able to determine the flow regime, the Reynolds number has to be calculated, the equation for Reynolds number is shown in Equation 3.15.

$$Re = \frac{\rho v D_p}{\mu} \tag{3.15}$$

Where D_p is the pipe diameter of the area where the fluid flows, v is the velocity of the fluid, and μ is the dynamic viscosity of the fluid. A flow can be considered laminar if the Reynolds number is below 2300, and turbulent if Reynolds number is above 4000. The interval in between is considered as the transition area, where the flow is combination of the two.

3.3.5 Turbulence model K-Epsilon

The K-Epsilon turbulence model is a two-equation model that solves transport equations for turbulent kinetic energy k and turbulent dissipation rate ϵ in order to determine the turbulent eddy viscosity. Eddy viscosity is a coefficient that relates the average shear stress in a turbulent flow to the vertical gradient of velocity. The eddy viscosity depends on the fluid density and distance from a wall, and can be described as shown in Equation 3.16

$$\mu_t = \rho C_\mu f_\mu k \Gamma \tag{3.16}$$

Where ρ is the density, C_μ is a model coefficient, f_μ is a damping function and Γ is the turbulent time scale (Siemens, 2017).

The two transport equations for k and ϵ is given in Equations (3.17) and (3.18),

$$\frac{\partial(\rho_m k)}{\partial t} + \nabla(\rho_m \vec{u} k) = \nabla\left(\frac{(\mu_m + \mu_t)}{\sigma_k}\nabla k\right) + k(G - \rho_m \epsilon) \tag{3.17}$$

$$\frac{\partial(\rho_m \epsilon)}{\partial t} + \nabla(\rho_m \vec{u} \epsilon) = \nabla\left(\frac{(\mu_m + \mu_t)}{\sigma_\epsilon}\nabla \epsilon\right) + \frac{\epsilon}{k}(C_1 G - C_2 \rho \epsilon) \tag{3.18}$$

where

$$G = \frac{\mu_m\left(\nabla\vec{u} + \nabla\vec{u}^T\right)}{\nabla\vec{u}} \tag{3.19}$$

and

$$\sigma_\epsilon = \frac{\kappa^2}{[0.3(C_1 - C_2)]} \tag{3.20}$$

$C_1 = 1.44$; $C_2 = 1.92$; $\sigma_k = 1.0$ and $\sigma_\epsilon = 1.3$, known as the turbulent Schmidt numbers, and κ is von Karman's constant (Balakin et al., 2017). These constants is universal, which makes it possible to use this model in various flow situations without calibration. This is one of the main advantages of the $k - \epsilon$ model (Olsen, 2007).

3.3.6 Convection

Heat transfer from convection transfers the thermal energy by means of diffusion and the movement of fluid from one place to another. In areas close to another surface where the velocity of the fluid is zero, heat transfer will only occur by diffusion. In areas were the fluid flow is different from zero, heat is transported downstream by the motion of the fluid. Convection is often referred to as natural or forced. Natural convection occurs in the gravitational field where the the temperature difference drives the convection from the high temperature to the low temperature fluid. In forced convection there is an external source like for example a pump, a fan, or the action from a propeller that will result in fluid movement, and will increase the rate of heat transfer across the surface. The heat transfer due to convection at a surface is described by Newtons law of cooling, end shown in Equation 3.21 (Siemens, 2017).

$$\dot{q} = h(T_s - Tref) \tag{3.21}$$

Where $\dot{q}$ is the local surface heat flux per unit area, h is the convective heat transfer coefficient, T_s is the surface temperature, and T_{ref} is the temperature of the fluid flowing over the surface (Siemens, 2017).

Chapter 4

Model description

This chapter consists of modeling the geometry, making an appropriate mesh, and setting up the physics for solving the governing equations for the computational fluid dynamics. The first case of interest is modeling a bladder-type accumulator which is to be validated by an experimental project executed by Stenhjem (2018) as well as an analytical approach developed by Hiis and Stenhjem (2017). The second, and third case is modeling a part of a barrier fluid system delivered by the cooperative company to get a better understanding of some abnormalities accruing when discharging.

4.1 Case 1, Single baldder accumulator

In this section the development of the model for the single bladder-type accumulator is described. First the geometry is presented, before the generation of mesh is described, then the boundaries and physics is show.

4.1.1 Geometry

The geometry used for modeling this case is made in STAR-CCM+. The model is based on a bladder accumulator used in an experimental project done by Stenhjem (2018), parallel to this study. This accumulator has an internal volume of 4 liters and is of the bladder-type. The model is made by making a sketch of the half accumulator, and then revolving this sketch 360 degrees to a full accumulator. The sketch and full accumulator is shown in Figure 4.1.

The outlet diameter is selected according to the valve openings in the experiments done by Stenhjem (2018), and there is chosen three different outlet areas. The areas and outlet diameters is shown in Table 4.1.

Experiment	Opening area	Outlet diameter
1	2.53 mm^2	1.79 mm
2	15.4 mm^2	4.43 mm
3	38.1 mm^2	6.97 mm

Table 4.1: Opening area and diameter corresponding to experiment.

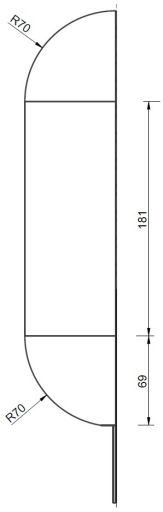

(a) Sketch of accumulator body.

(b) Revolved representation of accumulator body.

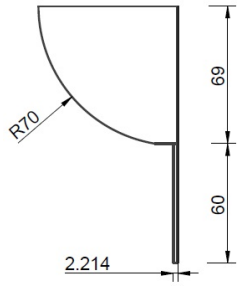

(c) Outlet sketch of accumulator.

Figure 4.1: Representation of sketch and geometry of bladder accumulator.

4.1.2 Mesh

The meshing consists of both surface and volume mesh, and is added in STAR-CCM+. The surface mesh is used to prepare the geometry for volume meshing, where the surface remesher was used. Surface remesher is used to improve the overall quality of the existing surface and optimize it for the volume mesh models. The remeshing is primarily based on a target edge length added by user (Siemens, 2017), a representation of the surface mesh is shown in Figure 4.2a.

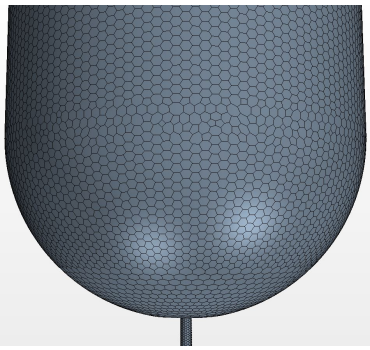

(a) Cylinder shell mesh.

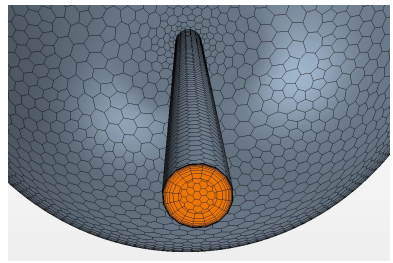

(b) Outlet and bottom mesh.

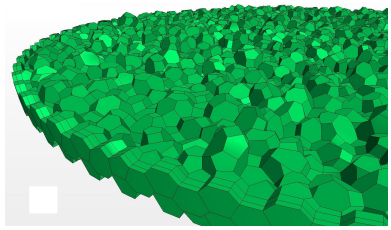

(c) Plane section of volume mesh.

Figure 4.2: Representation of mesh of the bladder accumulator.

Due to the geometry of the model, the volume mesh was created by using polyhedral cells with a generalized cylinder mesher, which generates extruded orthogonal cells along the cylindrical section of the geometry (Siemens, 2017). The overall volume mesh was also built with prism layers on the edge of the geometry to get an accurate solution of the turbulent regimes of the model. The prism layer mesher generates a orthogonal prismatic cells next to wall surfaces, this layer of cells is necessary to improve the accuracy of the flow solution (Siemens, 2017). Based on the dimensions of the outlet pipe, there were made a volumetric control to make the mesh smaller and more suited for the physical challenges occurring in this area of the geometry. The size of the computational cell of the outlet pipe in experiment 1 was set to 8 % of the base size, for experiment 2 and 3 this size was set to 50 % of the base size, and there were made 10 prism layers to account for the expecting turbulent flow, shown in Figure 4.2b. A visualization of the volume mesh with ten prism layers is shown in Figure 4.2c. The total cell count for experiment 1, 2 and 3 is 296341, 173078 and 266319 respectively.

Mesh independence

To ensure the accuracy of the physics in this model, the results have to be independent of the grid size. A mesh independence study was carried out to determined the best mesh size that can provide the most accurate results with the least amount of computational effort. The study was carried out by changing the base size of each cell, so different amounts of cells in the total geometry was obtained. The study consists of six different base sizes ranging from 1 mm to 6 mm, the mesh properties is shown in Table 4.2 and the profiles of the discharge is shown i Figure 4.3.

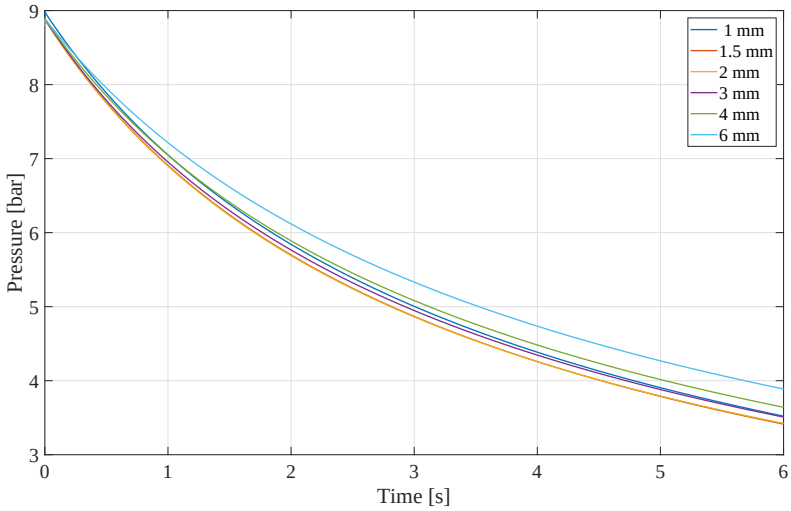

Figure 4.3: Discharge of pressure with different base sizes of cells.

From Figure 4.3, it can be seen that the number of cells do not have any significant impact on the results, Figure 4.4 shows a representation of the discrepancies of the different base sizes with respect to the result with highest cell count. The result with the lowest number of elements has the slowest discharge, while the second highest number of cells has the fastest discharge, with a maximum deviation between these two in pressure of 12.16 %. The mesh with base size of 3 mm, with a cell count of 161788, is discharging in between these two endpoints and can be considered as the optimal choice for further simulations based on computational time and effort.

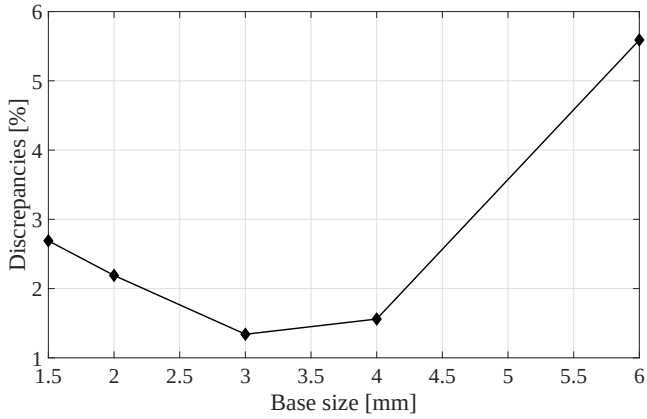

Figure 4.4: Average discrepancies with respect to base size of cells.

Base size	Number of cells	Avergage discrepancies	Maximum discrepancies
1 mm	3613573	0%	0%
1.5 mm	1118424	2.69%	3.34%
2 mm	542753	2.19%	2.77%
3 mm	161788	1.34%	2.15%
4 mm	89072	1.56%	2.78%
6 mm	27525	5.59%	8.49%

Table 4.2: Mesh independence properties, reference to base size of 1 mm.

4.1.3 Boundary and Physics

The model is equipped with two different boundary conditions, pressure outlet and wall boundaries. Pressure outlet was used since the pressure on the outside of the accumulator (backpressure) is a known value, this pressure is equal to atmospheric pressure. The wall boundary indicates the wall of the geometry and its conditions, and was treated as no-slip adiabatic with standard wall functions.

When simulating this case, the model was set up and initialized from charged conditions. The values in the initialization was obtained from experiments done by Stenhjem

(2018), the accumulator was pre-charged with air at 2 bar with initial volume of 2.5 l of fluid. The fluid inside is a mixture of water and glycol with a concentration of 10 % glycol, and a density of 1012.5 kg/m^3. The charge pressure was 8.9 bar and a temperature of 20°C in the gas when charged. The temperature increase when compressing the gas when charging was not taken into account for this model.

To be able to set the initial condition of the fluid level inside the accumulator a field function of the composition of the fluid had to be made. This field function makes it possible to set a wanted initial liquid height inside the accumulator, and reads as shown below

Volume_fraction_water = ($$Position[1]>liquid_height)?1.0:0.

and will return liquid phase in positions less than liquid_height, else the function will return gas phase.

Initially it is assumed that the capillary forces act as a physical divider of the two fluids inside the accumulator, the initial fluid level is shown in Figure 4.5.

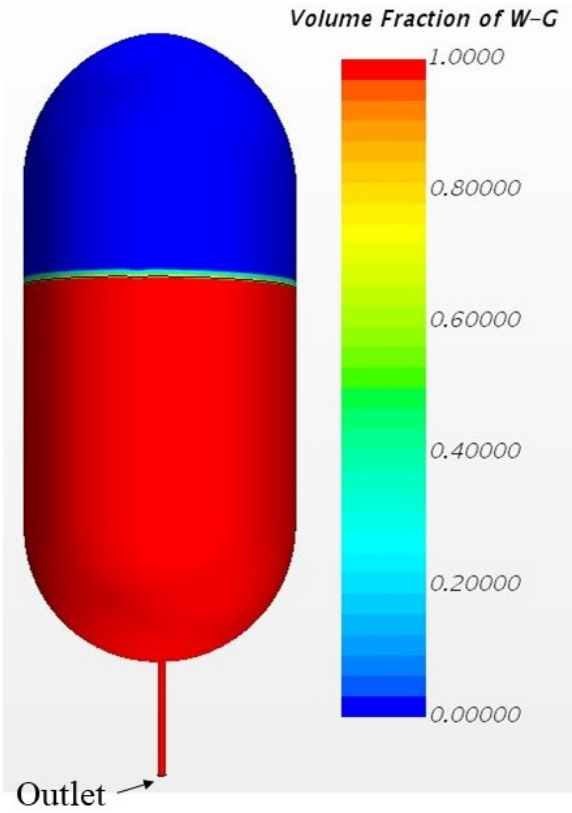

Figure 4.5: Initial volume fraction.

The model was set up by using the physical models in STAR-CCM+. In the accumulator, the two phase flow was modeled as segregated flow with Eulerian Multiphase model and Volume of Fluid as described in Section 3.3.3. The air is considered as an ideal gas, and the mixture of water and glycol is considered as constant density. The turbulent behavior of the flow is set to be calculated by the transport equations for the kinetic energy and the rate of energy dissipation in STAR-CCM+. In this model, the gravity, unsteady time domain, conservation of energy and the segregated fluid temperature models was taken into consideration.

The segregated flow model solves the flow equations (one for each component of velocity, and one for pressure) in a segregated or uncoupled manner. The model is designed for the use in a constant density regime, although it is capable to handle mildly compressible flows. The segregated fluid temperature model solves the total energy equation with temperature as the solved variable, enthalpy is then computed from temperature according to the equation of state (Siemens, 2017).

The turbulence model was selected due to the expecting turbulent flow regime in the outlet pipe of the accumulator. The Reynolds number can be calculated from Equation 3.15 in Section 3.3.4, a discharge from approximately 9 bar has a outlet velocity of 15 m/s. The corresponding Reynolds number can be calculated to be approximate 67000 which indicates that the flow is well inside the turbulent flow regime, and validates the use of the turbulent flow models.

4.2 Case 2: Generalized model

The generalized case described in this section is based on the two accumulators in the hydraulic power unit described in the introduction, but the accumulator volumes is scaled up by a factor of four. And consists of the modeling of the geometry, construction of mesh, and a description of the boundaries and physics used.

4.2.1 Geometry

The geometry made consists of a set of two accumulators placed in series, this model is based on the hydraulic power unit used in the barrier fluid system. The accumulators has an internal volume of 40 l each and is of the piston type. To be able to save computational time the geometry is cut in half, as shown in Figure 4.8b. Also from this figure the outlet nozzle can be seen. The outlet area of this nozzle is changed for the different studies in this case, all simulations conducted is presented in Table 5.1.

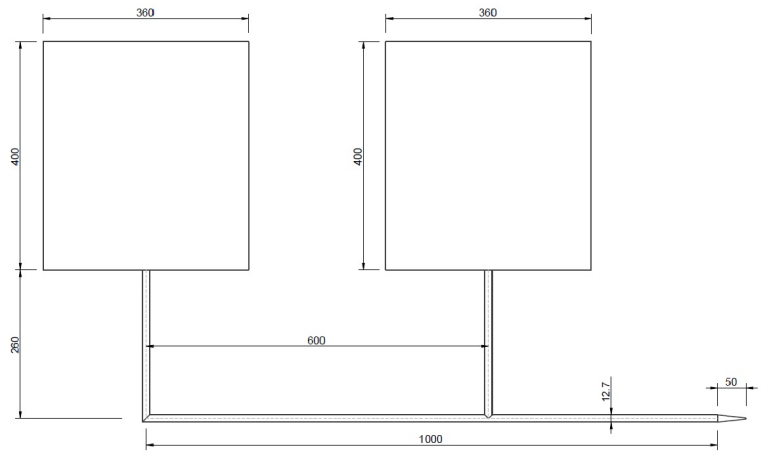

(a) Sketch of accumulator body.

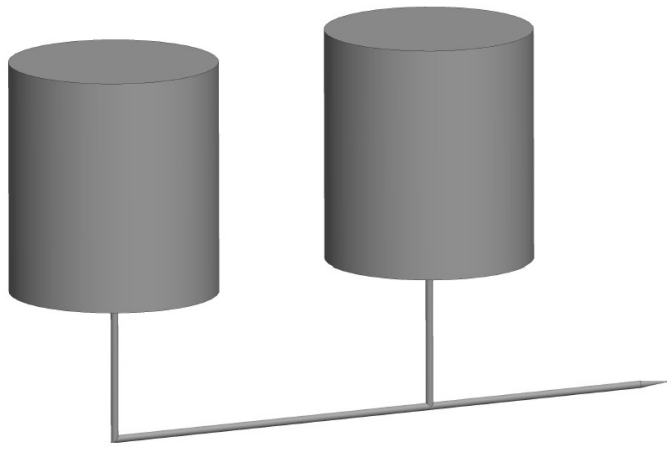

(b) Revolved representation of accumulator body.

Figure 4.6: Representation of sketch and geometry of bladder accumulator.

4.2.2 Mesh

The mesh constructed for the model of two accumulators is very similar to the mesh made for the model of one bladder accumulator. The surface mesh consists of a surface remesher, while the volume mesh is based on polyhedral cells and generalized cylinder mesher. The total base size for the computational cell is 6 mm, which is based on the mesh independence study conducted and shown in Section 4.1.2, and to keep the cell count to a minimum due to computational power. This size is applied to the accumulator bodies, for the piping, the base size is set to 3 mm, while for the outlet nozzle the base size varies based on the outlet radius.

The base size for the outlet radius of 1, 2, 3, 4 and 5 mm is 0.3, 0.6, 1.5, 1.2 and 1.2 mm respectively.

Outlet radius	Accumulator base size	Pipe base size	nozzle base size	Number of cells
1 mm	6 mm	3 mm	0.3 mm	509427
2 mm	6 mm	3 mm	0.6 mm	437062
3 mm	6 mm	3 mm	1.5 mm	416977
4 mm	6 mm	3 mm	1.2 mm	326815
5 mm	6 mm	3 mm	1.2 mm	485873

Table 4.3: Mesh properties for the different geometries studied in the generalized case.

For the accumulator bodies, close to the wall there is two prism layers, while for the pips there are 20 prism layers, and for the outlet nozzle there is 5 prism layers. The different cell count and mesh properties is shown in Table 4.3. The generated mesh for one of the two accumulators, as well as the mesh of both the pipe and nozzle is shown in Figure 4.7.

Figure 4.7: Representation of mesh for the outlet and one of the two accumulators.

To be able to ensure the quality of the mesh there were ran an mesh diagnostic report in STAR-CCM+ for the all mesh generated. The report checks for mesh and face validity and volume change statistics, in addition to this diagnostic report the skewness angles

of the cells was studied. The mesh validity checks for invalid cells, cells with zero or negative volume and unclosed cells. The face validity is an area-weighted measure of the correctness of the normal of the face relative to their attached cells centroid. In a good cell the face normals point outwards and away from the centroid, while for a bad face validity one or more of the face normals point inwards towards the cell centroid. From the report, all cells with face validity of less than 1.0 is considered as bad cells (Siemens, 2017).

The volume change statistics describes the ratio of the volume of a cell to the largest neighboring cell, and as mentioned in Section 3.3.2, all cells with a volume change of 0.001 or less is considered as bad cells (Siemens, 2017).

To investigate the skewness angle in the mesh generated a plot that shows the distribution of the amount of cells with respect to the skewness angle. The skewness angle is the angle between the face area vector and the vector connecting the two cell centroids. If this angle is equal to zero, the mesh is perfectly orthogonal, a skewness angle of 85°or greater is considered bad cells (Siemens, 2017).

For all generated mesh in this study the diagnostics of the mesh shows that the mesh was valid, and had no cells considered as bad.

4.2.3 Boundary and Physics

The geometry in this model has three different boundary conditions, pressure outlet and wall boundaries, equal to the model developed in Section 4.1, and a symmetry plane boundary. The symmetry plane boundary represents an imaginary plane of symmetry in the model, and the solution obtained with this boundary is identical to the solution that would be obtained by mirroring mesh about the symmetry plane (Siemens, 2017). The outlet pressure for this case varies between three different backpressures shown in Table 5.1. The walls are treated as no-slip with smooth surfaces and with convection in the accumulator bodies with a heat transfer coefficient of 3 W/m^{2}K, which is the most typical value for the environmental conditions inherent for the considered industrial case.

When simulating these cases the model was set up and initialized from charged conditions. The different initial values was provided by the cooperative company. The two accumulators has different pre-charge pressures, 30 and 19 bar for the left and right accumulator respectively, with an equal charge-pressure of 35 bar. This indicates that the initial volume is different for the two accumulators, the fluid volume in the different accumulators is approximately 4.171 l and 14.145 l, the different volumes is calculated by Equation 4.1 where P_0 and V_0 is the pre-charge pressure and volume respectively, P_1 and V_1 is charge pressure and volume, the initial volume is shown in Figure 4.8a.

$$P_0 V_0^{\gamma} = P_1 V_1^{\gamma} \tag{4.1}$$

Due to the difference in pre-charge, the temperature in the gas section will be different for the two accumulators when charged. The temperature in the two respective accumulators is calculated by use of Equation 4.2.

$$T_0 V_0^{\gamma-1} = T_1 V_1^{\gamma-1} \tag{4.2}$$

Where T_0 is the initial temperature before the accumulators is charged and is equal to 20°C, and T_1 is the gas temperature when charged. The gas temperature for the left

accumulator is 33.2°C and right accumulator has the temperature of 75.6°C when charged which is equal for all the cases simulated.

To be able to set the desired initial conditions for the accumulators there were made some field functions in STAR-CCM+. The code made for setting the wanted level inside the two accumulators reads as follows:

level = ($$Position[0]<${distance})?${level_accu_A}:${level_accu_B}

which represents that for distance, which is set in between of the two accumulators, is less than position [0], which is the value of distance, will present the level inside accumulator A, else the level will be sett to the level of accumulator B. For the different temperatures inside the two accumulators, the field function is defined as shown below:

Gas_temp = ($$Position[0]<${distance})?306.2:348.6

where if the position is less than distance, the field function will return a temperature of 306.2 K, else it will return 348.6 K. To ensure that these temperatures only is applied to gas inside the accumulators, another field function was made and defined as:

(${VolumeFractionN2}>0.9)?$Gas_temp:293

which will apply the different temperatures only if the volume fraction of Nitrogen is greater than 0.9, else the field function will return a temperature of 293 K.

The physical models in this case is close to identical to the physics described in Section 4.1.3. The difference in this model is the fluid and gas used, the gas used is nitrogen treated as an ideal gas, with standard properties located in the species library in STAR-CCM+. The fluid used is based on an hydraulic oil, Shell Morlina S2 BL5, the properties for this oil is shown in Table 1.1.

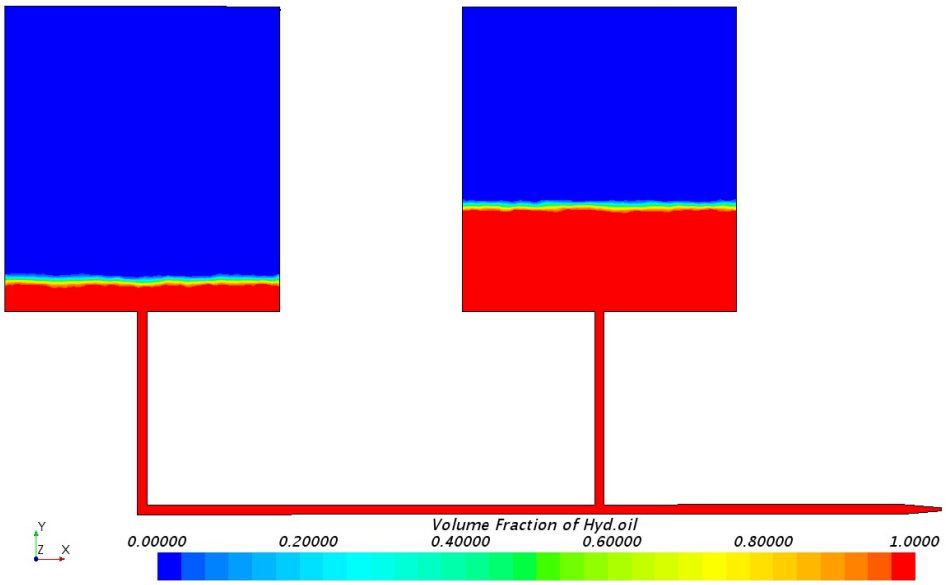

(a) Initial volume fraction for the two barrier fluid accumulators.

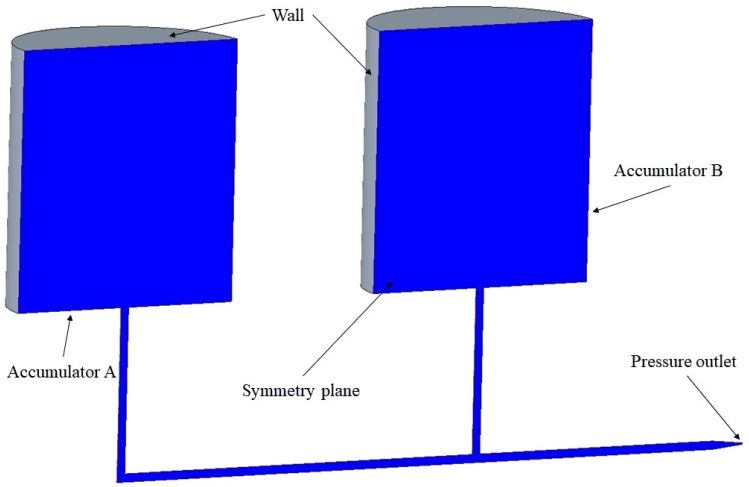

(b) Representation of geometry used for simulation.

Figure 4.8: Initial volume fraction and boundary representation.

4.3 Case 3: Industrial model

The case described in this section is very similar to the generalized model described in Section 4.2. The difference in these two cases is the size of the accumulator bodies, and

small changes in the mesh generated.

4.3.1 Geometry

The geometry made in this model is also based on the barrier fluid system HPU. The volume of the accumulators used is 10 l each with a diameter of 0.18 m, and a height of 0.4 m. Both accumulators is of the piston type, and has the same internal volume used in the industrial system. The diameter of the pipes is 12.7 mm, and the outlet area of the nozzle is 12.56 mm^2, shown in Figure 4.9.

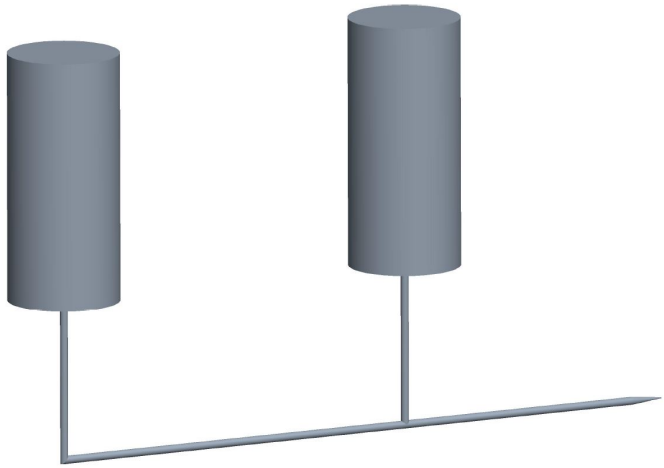

Figure 4.9: Revolved representation of accumulator body.

4.3.2 Mesh

The mesh generated is close to identical to the mesh made in generalized model, the difference is the cell base size for the accumulator bodies which is in this model 4 mm, based on the mesh independence study described in Section 4.1.2 and to keep a cell count as low as possible with the least amount of computational power which will provide the best result. There where also made some changes to the mesh in the nozzle and the prism layers in the pipes. The prism layers was changed to 10 layers for both the pipes and nozzle, and the cell base size was set to 0.32 mm for the nozzle, while for the pipes, mesh size was set to 3 mm. This mesh gave a total cell count of 504015 cells for this geometry.

4.3.3 Boundary and Physics

Boundaries used for the model in this case is equal to the boundaries described in Section 4.2.3 above. The outlet pressure for this case was varied between 30.7, 25 and 20 bar, and the pre-charge pressure was 30 and 19 bar for the two accumulators. The accumulator with the lowest pre-charge has a hydraulic fluid volume of 3.537 l when charged at 35 bar, the second accumulator with the highest pre-charge has a volume of 1.043 l at charge

pressure. These volumes is calculated adiabaticly by Equation 4.1. When it comes to the charge temperature of the gas in these accumulators, the temperatures is equal to the generalized case due to the compression rate is equal for the two cases. From Section 4.2 the order of the pre-charge was kept constant throughout all the simulations, where accumulator A had the highest pre-charge, while accumulator B had the lowest pre-charge. in this case, the pre-charge order was changed to be able to analyze the effect how the system will react to this modification, the two different pre-charge settings is shown in Figure 4.10, Figure 4.10a shows the first pre-charge setting, while Figure 4.10b shows the second setting where the order of pre-charge has been changed. The physical models used is identical to the physics used in Section 4.2.3. To be able to set the initial conditions, the same field functions described in Section 4.2.3 was used. To change the order of the pre-charges as shown in Figure 4.10, the signs of ”less than”, was replaced with ”greater than”.

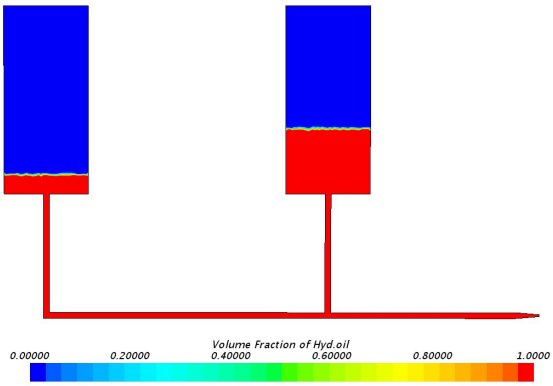

(a) Initial volume fraction for pre-charge setting 1.

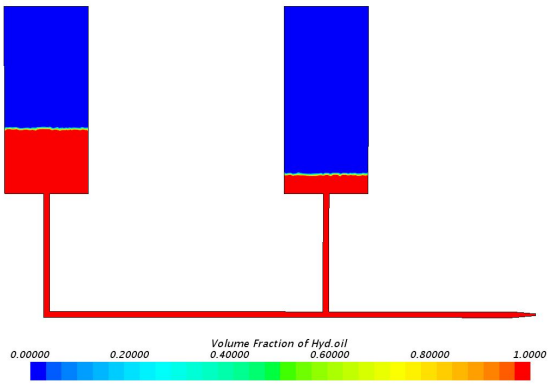

(b) Initial volume fraction for pre-charge setting 2.

Figure 4.10: Initial volume fractions for the industrial case.

4.3.4 Theoretical Model

To be able to validate model made in STAR-CCM+ there is developed an theoretical equation of the pressure discharge in the accumulators to be be compared to the pressure profiles obtained from the simulations executed.

The equation developed is based on accumulator discharge through a nozzle. Due to the complexity of the system the theoretical discharge is treated as isotherm. The volume flow out of an accumulator can be described by Equation 4.3, while volume flow through the nozzle can be modeled by Equation 4.4.

$$Q = \frac{dV}{dt} = \frac{-\alpha}{P^2}\frac{dP}{dt} \tag{4.3}$$

$$Q = A\psi\sqrt{\frac{2(P - P_B)}{\rho}} \tag{4.4}$$

Where $\alpha = P_0 V$ where P_0 is the charge pressure and V is the volume of gas when charged, P_B is the pressure outside of the nozzle (backpressure), ψ is the discharge coefficient and can be approximated by Equation 4.5.

$$\psi = \frac{1}{1.5 + 13.74\sqrt{\frac{l}{dRe}}} \tag{4.5}$$

Where l is the nozzle length, d is half of the nozzle diameter and Re is Reynolds number calculated by Equation 3.15 (Brautaste, 2013). To simplify Equation 4.4,the constant values is set as $\beta = A\psi\sqrt{\frac{2}{\rho}}$. The volume flow out of the accumulator has to be equal to the volume flow through the nozzle as:

$$\frac{-\alpha}{P^2}\frac{dP}{dt} = \beta\sqrt{P - P_B} \tag{4.6}$$

Rearranging Equation 4.6 and getting the differential equation:

$$\int \frac{dP}{P^2\sqrt{P - P_B}} = \int \frac{-\beta}{\alpha} dt \tag{4.7}$$

The solution to the differential Equation 4.7 is shown in Equation 4.8

$$\frac{\tan^{-1}\left(\frac{\sqrt{P-P_B}}{\sqrt{P_B}}\right)}{P_B^{1.5}} = \frac{-\beta t}{\alpha} + K \tag{4.8}$$

Where K is the combined integral constant which is calculated from initial conditions where $t = 0$ and $P = 35$ bar.

To solve for P in Equation 4.8, a code in Matlab was developed due to the complexity of the analytic solution, this code can be found in Appendix A.1.1.

Since the model developed in STAR-CCM+ consists of a set of two accumulators in series, the theoretical equation had to be adapted to the this system. Due to the development of this equation only consider one accumulator, there had to be taken some assumptions

in consideration when producing the pressure profiles. The combined pre-charge pressure was set to 19 bar, the volume of gas in the theoretical accumulator was calculated from the total mass obtained from the two accumulators used in STAR-CCM+ by use of the ideal gas law shown in Equation 4.9

$$m = \frac{PVM}{RT} \tag{4.9}$$

Where m is the mass of the gas, R is the gas constant and M is the molecular weight of the gas. The total mass of Nitrogen in the two accumulators are calculated from pre-charge pressure. This mass is then used in calculation of the total volume of gas in the theoretical accumulator. All calculations done is shown in Appendix A.

Chapter 5

Results

In this chapter the results from all cases studied is presented. First the results obtained from the bladder-type accumulator case, then the generalized case and industrial case is presented.

5.1 Bladder-type Accumulator

For the numerical method to obtain the desired values, the solver was set to 1 ms per time step with temporal discretization of first order. To be able to analyze the results obtained from STAR-CCM+ the pressure and velocity profile was extracted from STAR-CCM+ and plotted by using Matlab. The accumulator was discharged through three different valve openings, shown in Table 4.1. The pressure and velocity profiles for the different outlet areas is shown in Figures 5.1 to 5.3.

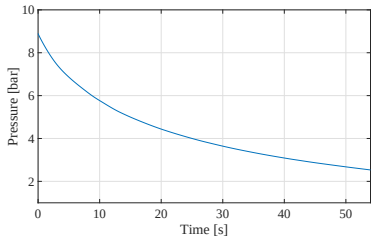

(a) Pressure profile through opening nr 1.

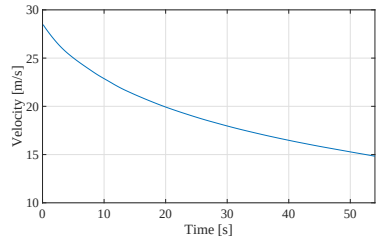

(b) Velocity profile of opening nr 1.

Figure 5.1: pressure and velocity profile of opening nr 1.

The results obtained from the simulation of opening nr 1, where the outlet area of the accumulator is 2.53 mm^2 is shown in Figure 5.1. Figure 5.1a shows the pressure profile, while Figure 5.1b shows the velocity profile. As displayed in the figures below the discharge time of the low pressure accumulator is approximately 55 second. The results collected from the simulation of opening nr 2, where the opening area is 15.5 mm^2 is

shown in Figure 5.2 below. Figure 5.2a shows the pressure profile, while Figure 5.2b shows the velocity profile while discharging. From the figures it can be seen that the discharge time is approximately 9 seconds. Figure 5.3 represents the velocity and pressure profiles where the outlet area is 38.1 mm^2. When this figure is studied, it is observed that the time for total discharge is approximately 3.4 seconds.

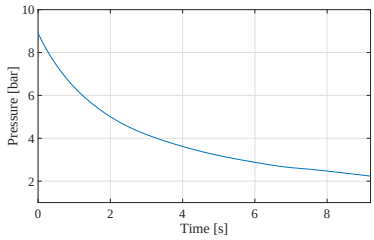

(a) Pressure profile through opening nr 2.

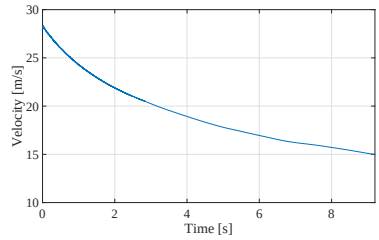

(b) Velocity profile of opening nr 2.

Figure 5.2: pressure and velocity profile of opening nr 2.

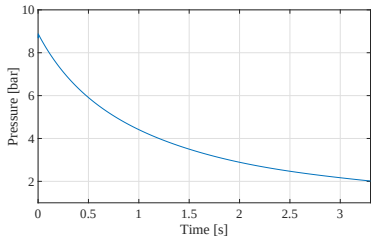

(a) Pressure profile through opening nr 3.

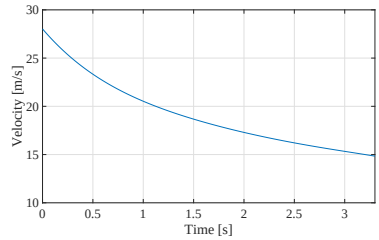

(b) Velocity profile of opening nr 3.

Figure 5.3: pressure and velocity profile of opening nr 3.

The discharging profiles of the three outlet opening areas all have the exponential decay. This type of profile is due to the pressure difference of gas inside the accumulator and the pressure on the outlet of the pipe. When the pressure is discharged the rapid pressure drop in the beginning will lead to a more rapid drop of temperature in the accumulator, which will affect the pressure inside the accumulator.

When studying the different velocity profiles, the highest and lowest velocities is equal for all three cases. The reason for the equal velocity profile is that velocity has a direct correlation to the volume flow out of the accumulator, $Q = v \times A$, where Q is volume flow, v is velocity and A is the outlet area. And since the initial volume in the accumulator is equal for all cases the velocity profile will also look similar.

To be able to control if the model developed in STAR-CCM+ is credible, was it validated by the theoretical approach and the experimental modeling done by Stenhjem (2018) for the three different outlet areas shown in Table 4.1. The experimental setup had a precharge of 2 bar which means that the accumulator is empty at 2 bar when discharged. The discrepancies of pressure at a given time can be calculated by using Equation 5.1. In Table

6.1 the average and maximum discrepancies is listed.

$$\delta = \frac{p_{CFD} - p_{theoretical}}{p_{theoretical}}$$
$$\delta = \frac{p_{CFD} - p_{experimental}}{p_{experimental}} \tag{5.1}$$

Where δ is the discrepancy of pressure, p_{CFD} is pressure for the CFD, $p_{experimental}$ is the experimental pressure, and $p_{theoretical}$ is the pressure of the theoretical solution.

Figure 5.4 presents the pressure profile for analytical, experimental and CFD can be seen. The figure shows that the experimental and analytical profile is very similar, while the profile obtained from the simulation has a bit slower discharge. The average discrepancies to the analytical approach is approximately 3.5 % and 4.3 % to the experimental data, where the maximum discrepancies to the experimental and analytical approach is 8.3 % and 9.0 % respectively.

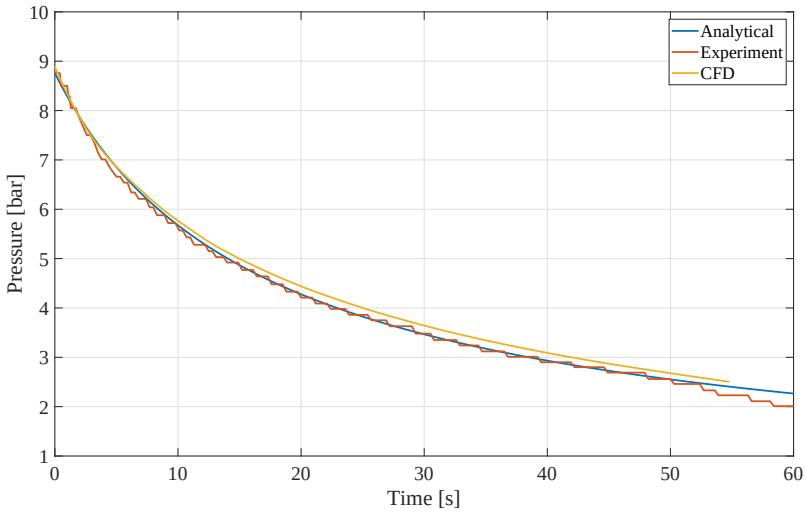

Figure 5.4: Comparing analytical, experimental and CFD discharge, opening nr 1.

In Figure 5.5 the three different solutions is compared for outlet area 15.4 mm^2. As can be seen from the profiles the differences of discharge is very small. The CFD is following the analytical curve exceptional, and has an average discrepancy of only 1.3 % and a maximum of approximately 2.2 %. When comparing to the experimental discharge the CFD model is not so far off with the average deviation of 7.0 % and a maximum of approximately 21.0 %.

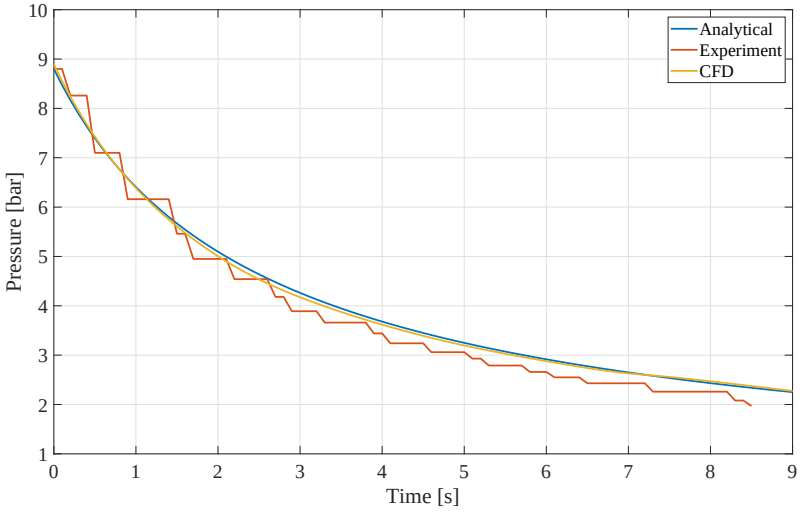

Figure 5.5: Comparing analytical, experimental and CFD discharge, opening nr 2.

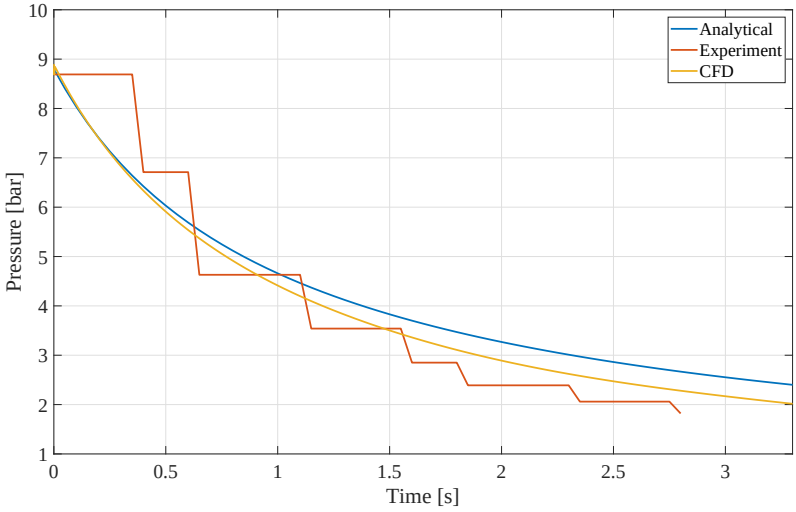

Figure 5.6: Comparing analytical, experimental and CFD discharge, opening nr 3.

The pressure profile of the three different approaches, analytical, experimental and simulation for the outlet opening area of 38.1 mm^2 is shown in Figure 5.6. For the results obtained the discrepancies of the pressure profiles is significantly larger for this area compared with the two other outlet areas. The average deviation to the experimental results is approximately 12.6 %, and a maximum of 27.9 %. As for the discrepancies to the

analytical results the average is 6.9 %, with a maximum of 13.6 %.

5.2 Generalized Model

To obtain the desired values from the numerical method, the solver was set to 0.5 ms per time step with temporal discretization of first order. From STAR-CCM+ the desired values in the system was extracted and plotted by use of Matlab. The values shown in this section is made dimensionless and plotted in a logarithmic scale. The y-axis corresponding to the pressure, and the x-axis which corresponds to the time is calculated as shown in Equation 5.2.

$$\begin{aligned} y - axis &= ln\frac{p}{p_0} \\ x - axis &= ln\frac{t}{\omega} \end{aligned} \tag{5.2}$$

Where p is the pressure at a given time, p_0 is the charge pressure, $\omega = V/Q$, where V is the total volume of one accumulator, and Q is the theoretical volume flow through a nozzle calculated by Equation 4.4. The profiles for each simulations obtained from this conversion was plotted with the corresponding linear regression, shown in Appendix B. From the linear regression the angle, φ, between the x-axis and the liearized profile was obtained, and listed in Table 5.1 together with tan(φ) and the corresponding Reynolds number. The Reynolds number was calculated by Equation 3.15 based on the theoretical maximum volume flow, Q, used in the dimensionless x-axis. Figure 5.7 shows the scatter representation of the dimensionless results, where values gathered from all cases is compered to each other. In this figure it is shown that when the discharge time decreases, the velocity through the outlet nozzle will increase which will result in a higher Reynolds number. Figure 5.7 also shows that there is similarities between the generalized and industrial cases, as well as the compared case were only one bladder-type accumulator is used. To better compare the results a exponential trendline from the generalized case was included in the figure, and modeled as: y = 0.4523e$^{-2.34\times10^{-5}x}$. The greatest deviation from the bladder-case to the system of two accumulators is observed where the opening area is largest, which gives the greatest Reynolds number. The values for the industrial case, and the bladder-type accumulator case used in Figure 5.7 is shown in Tables 5.2 and B.1 respectively.

All simulations conducted together with the angle φ, tan(φ) and the corresponding Reynolds number is presented in Table 5.1. The case marked with **base**, is the base case simulation. From this case only one parameter was changed per simulation.

Outlet area	Backpressure	Ambient Temperature		φ	tan(φ)	Re
78.54 mm^2	30.7 bar	20°C		3	0.05	37750
50.26 mm^2	30.7 bar	20°C		8	0.14	30200
28.27 mm^2	30.7 bar	20°C		13	0.23	22650
		4°C		17	0.31	15100
12.56 mm^2	30.7 bar	12°C		16.5	0.30	15100
		20°C	(**Base**)	16	0.29	15100
		27°C		15.5	0.28	15100
12.56 mm^2	25 bar	20°C		19	0.34	23027
12.56 mm^2	20 bar	20°C		17.5	0.32	28202
12.56 mm^2	0 bar	20°C		12	0.21	43080
3.14 mm^2	30.7 bar	20°C		19	0.34	7550

Table 5.1: All simulations conducted together with the angle φ, tan(φ) and the corresponding Reynolds number.

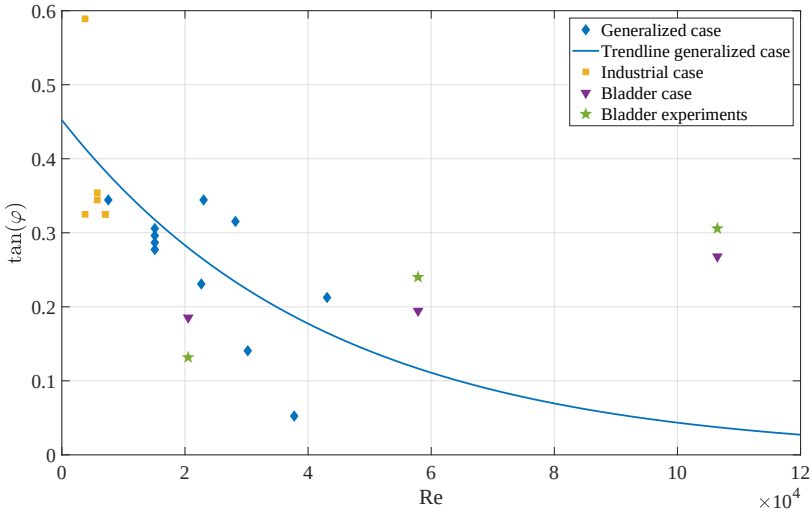

Figure 5.7: Representation of tan(φ) vs corresponding Reynolds number, where "Generalized case" represents the results form the case of two 40 l accumulators in series, "Industrial case" is the results from the case of two 10 l accumulators in series, "Bladder case" represents the results of a single 4 l accumulator, and "Bladder experiments" is the experimental results of the same 4 l bladder accumulator.

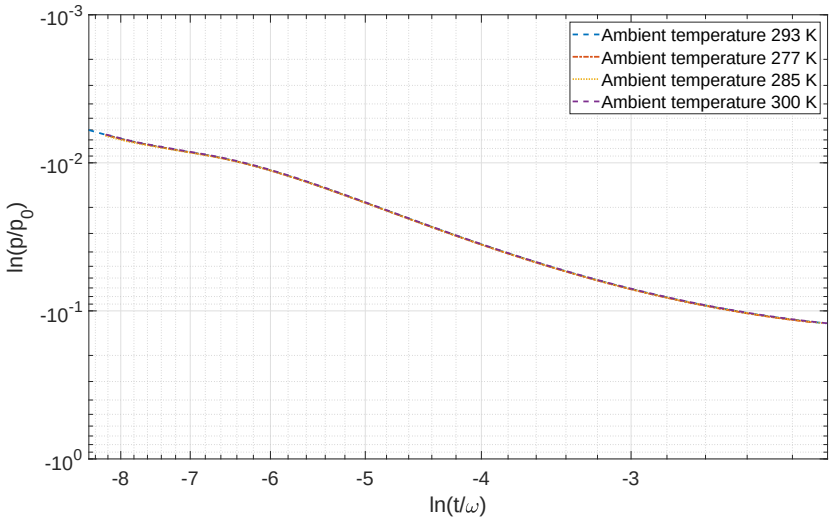

Figure 5.8: Dimensionless logarithmic plot where the ambient temperature is changing.

From Figure 5.8 the compared profiles for simulations where the outlet area and back-

pressure was kept constant, and only changing the ambient temperature is shown in a dimensionless manner in a logarithmic plot. As shown in this figure the deviation of the discharge profiles with respect to ambient temperature is very small, and looks almost identical.

Illustrated in Figure 5.9 the dimensionless representation is compared for simulations where the backpressure and ambient temperature was kept constant at 30.7 bar and 293 k respectively, while changing the outlet area as shown in Table 5.1. From this plot it can be seen that the deviation in discharge time differs from each other. It can be seen that the difference to the base case is larger when the outlet area is increased. Simultaneously the discharge through the smallest outlet area is very close to the base case, while the discharge through the nozzle with a outlet area of 28.27 mm^2 deviates more, even though the outlet diameter is increased/decreased with the same size in both directions.

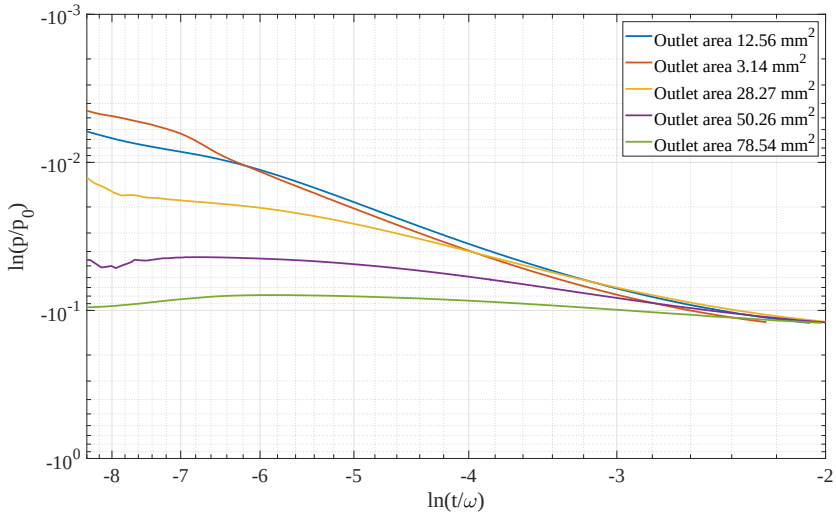

Figure 5.9: Dimensionless logarithmic plot where the outlet area is changing.

Figure 5.10 shows the compared profiles for the dimensionless values obtained from the simulations conducted while changing the backpressure and keeping the ambient temperature and outlet area constant at 273 K and 12.56 mm^2 respectively. When changing the backpressure in the system, the pressure profiles indicates that the discharge of the accumulator is highly effected by the lack of restrictions when discharged.

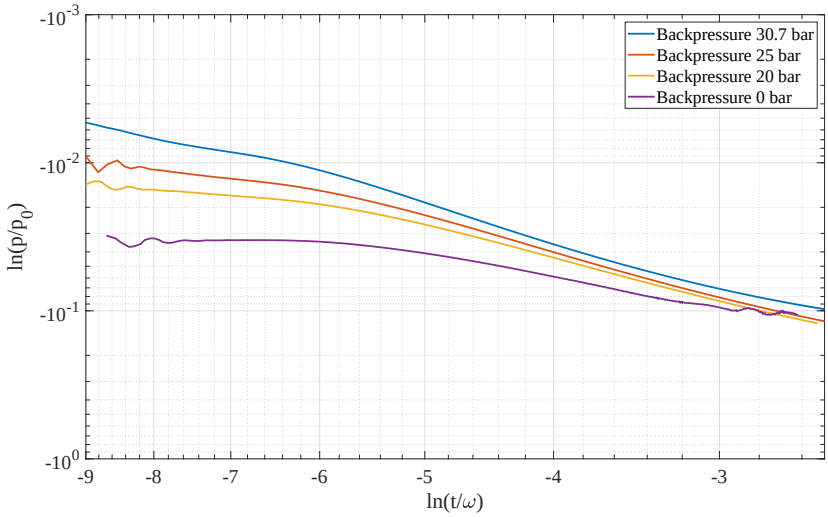

Figure 5.10: Dimensionless logarithmic plot where the backpressure is changing.

5.3 Industrial Model

When simulating the industrial case with smaller accumulators the solver was set to 1 ms per time step, with temporal discretization of first order to obtain the desired values from the numerical method. When computing these cases the discharge time, even though the outlet area is the same as the base case in the generalized case, is about 4 times as fast. The results presented in this section consists of simulations where the ambient temperature and outlet area was kept constant, and only changing the backressure. There were chosen three different backpressures, 30.7, 25, and 20 bar. These three different simulations were then conducted again after changing the pre-charge setting, as described in Section 4.3.3. From STAR-CCM+ the different pressure profiles from accumulator A and B, as well as the pressure obtained from the outlet pipe was extracted, and plotted in Matlab. The temperature profiles from the gas domain within the two accumulators was also extracted and plotted in this section.

Figure 5.11 shows the pressure and temperature profiles from the case where the back-pressure was set to 30.7 bar, and with pre-charge setting 1, from the result obtained the discharge time is approximately 5.7 seconds whereof the first 0.5 seconds there appears to be a more rapid pressure drop in accumulator B and in the outlet pipe than in accumulator A.

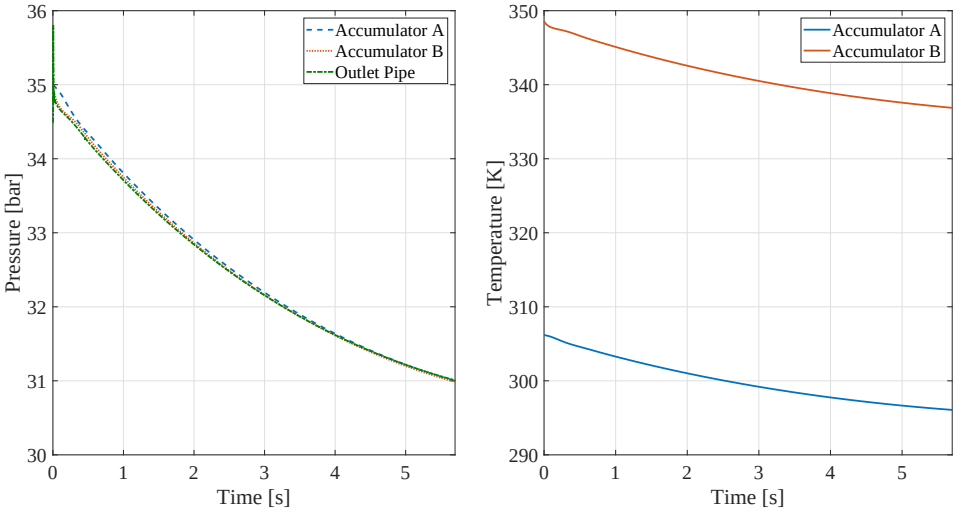

Figure 5.11: Pressure and temperature profiles for pre-charge 1, outlet are 12.56 mm^2 backpressure 30.7 bar and ambient T = 293K.

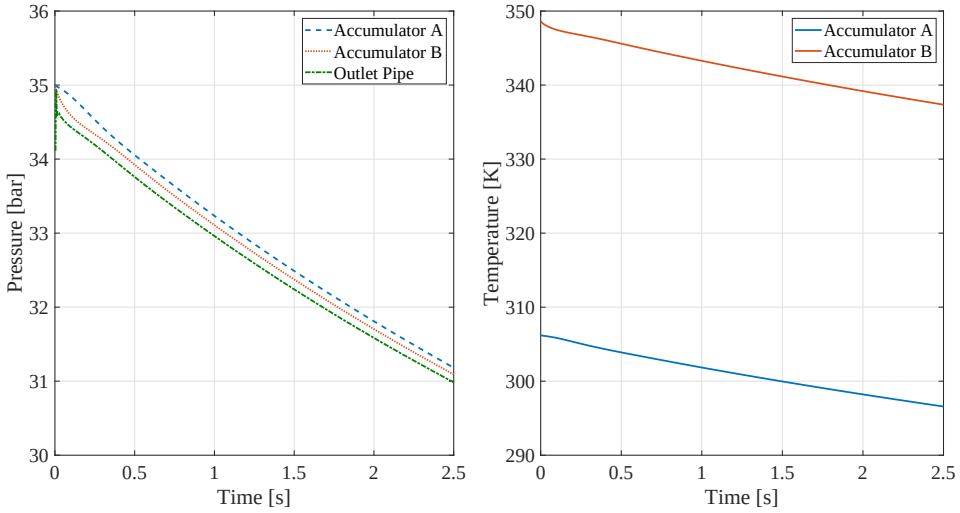

Figure 5.12: Pressure and temperature profiles for pre-charge 1, outlet are 12.56 mm^2 backpressure 25 bar and ambient T = 293K.

The figure shown in Figure 5.12, represents the pressure and temperature profiles when discharging the system with a backpressure of 25 bar with pre-charge setting 1. As can be seen from the figure the total discharge time for the system is approximately 2.5 seconds,

also this computation experiences a larger pressure drop in the first part of discharge in accumulator B and in the outlet pipe.

Figure 5.13 displays the profiles of pressure and temperature decrease from discharge of the system with a backpressure of 20 bar, with pre-charge setting 1. The total discharge time of the system is approximately 2 seconds, with the same pressure drops experienced in this case as well.

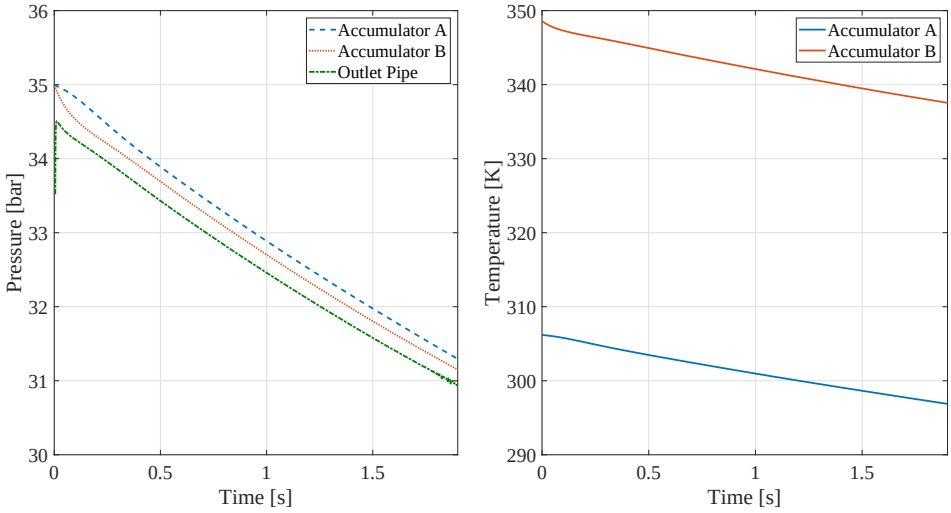

Figure 5.13: Pressure and temperature profiles for pre-charge 1, outlet are 12.56 mm^2 backpressure 20 bar and ambient T = 293K.

When discharging this system with different backpressures it appears that both the pressure and temperature profiles is similar for the different cases, but where the rapid pressure drop in the beginning is larger for the system where the flow restrictions in the outlet nozzle is smallest.

Further the results obtained from simulations conducted by changing the pre-charge order to pre-charge setting 2 as shown in Figure 4.10b. From Figure 5.14 the discharge profiles from the case simulated with backpressure of 30.7 bar and pre-charge setting 2 is displayed. Observably from these profiles the discharge time is approximately 5.7 seconds, which is very similar to the discharge time as obtained in Figure 5.11. Some of the differences between the two cases is that the accumulator with the lowest pre-charge, and highest charge temperature will not have the rapid pressure and temperature drop in the beginning of the discharge, which is a very intriguing effect.

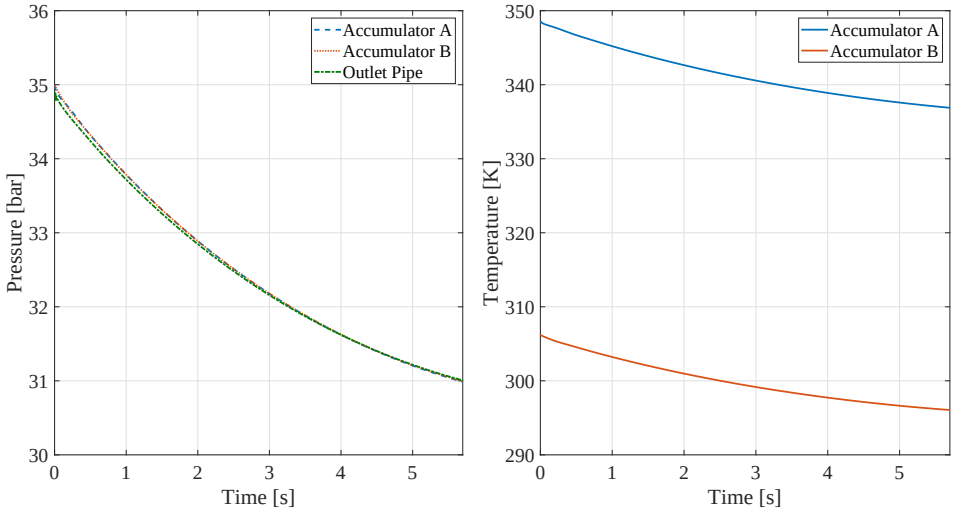

Figure 5.14: Pressure and temperature profiles for pre-charge 2, outlet are 12.56 mm^2 backpressure 30 bar and ambient T = 293K.

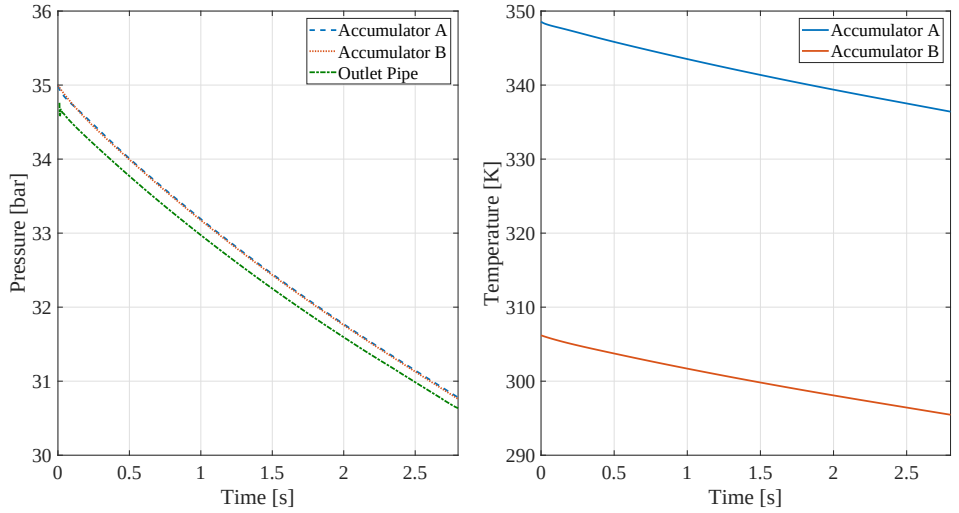

Figure 5.15: Pressure and temperature profiles for pre-charge 2, outlet are 12.56 mm^2 backpressure 25 bar and ambient T = 293K.

The next case studied is the discharge with pre-charge setting 2 and backpressure of 25 bar, the profiles is shown in Figure 5.15. Obtained from this figure is a discharge time of approximately 2.7 seconds, which also is very similar to the same case with different

pre-charge setting presented in Figure 5.12. Also here the difference between the two is the rapid pressure drop in the accumulator with the highest initial gas temperature. But the pressure obtained from the measuring point in the outlet pipe is significantly lower than the pressure observed in the two accumulators.

In Figure 5.16 the pressure and temperature profiles from discharging the system with a backpressure of 20 bar and pre-charge setting 2 is obtained. According to this figure the total discharge time is approximately 2 seconds, with the same profile pattern as obtained from Figures 5.14 and 5.15, but the pressure from the outlet pipe is further from the pressures obtained in accumulator A and B.

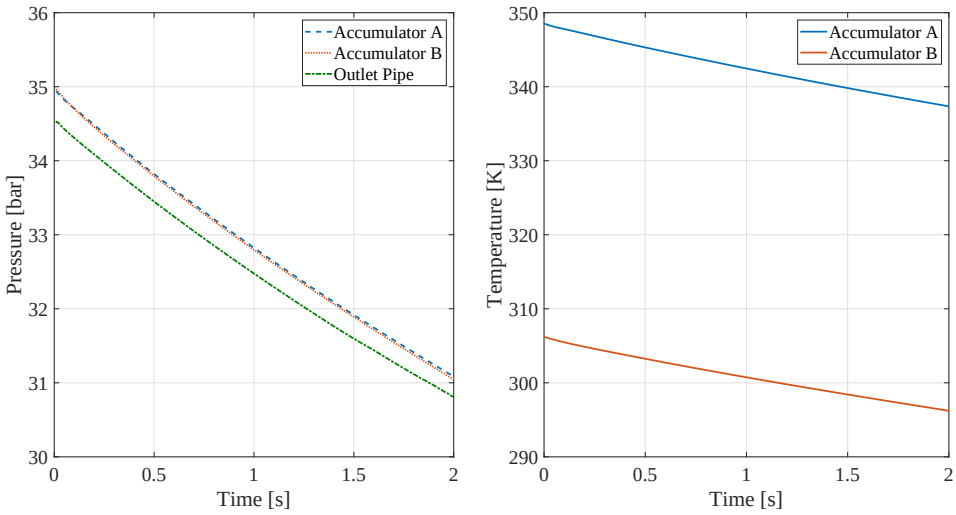

Figure 5.16: Pressure and temperature profiles for pre-charge 2, outlet are 12.56 mm^2 backpressure 20 bar and ambient T = 293K.

The cases studied in the current section has similar results as the generalized case when it comes to the pressure and temperature profiles obtained. The effect that is of interest is when changing the pre-charge setting the pressure profiles will act more stable in all three cases studied, without the rapid pressure drop in the accumulator with the highest initial temperature. This observation is studied in more detail in Section 6.3.

Based on all simulations conducted in this case, the angle, φ, was extracted from the dimensionless plots as done for the general case described in Section 5.2, the figures are shown in Appendix B.3. All cases simulated in this section, together with the angle φ, $\tan(\varphi)$ and the corresponding Reynolds number is shown in Table 5.2. The results of $\tan(\varphi)$ and the corresponding Reynolds number is compared and plotted in Figure 5.7.

Outlet area	Pre-charge setting	Backpressure	φ	tan(φ)	Re
12.56 mm^2	1	30.7 bar	30.5	0.59	3775
12.56 mm^2	1	25 bar	19	0.34	5757
12.56 mm^2	1	20 bar	18	0.32	7051
12.56 mm^2	2	30.7 bar	18	0.32	3775
12.56 mm^2	2	25 bar	19.5	0.35	5757
12.56 mm^2	2	20 bar	18	0.32	7051

Table 5.2: All simulations conducted together with the angle φ, tan(φ) and the corresponding Reynolds number.

Chapter 6

Discussion

In this chapter the results from the three cases modeled is discussed, first the case of one bladder-type accumulator, then the systems of two piston-type accumulators.

6.1 Bladder-type

	Analytical		Experiment	
Opening area	Avg	Max	Avg	Max
2.53 mm^2	3.52 %	5.41 %	4.35 %	13.26 %
15.4 mm^2	1.30 %	2.19 %	7.00 %	21.01 %
38.1 mm^2	6.88 %	13.61 %	12.57 %	27.86 %

Table 6.1: Descripancies to CFD.

As can be seen from the results listed in Table 6.1, the maximum discrepancies to the experiments is significantly larger than for the analytical solution. A point of interest for the slower discharge in the CFD model can be caused by the fact that the model made does not account for the temperature increase in the accumulator when charged. The initialized charge temperature was set equal to the temperature of the whole system. When the accumulator is discharged, the gas temperature will decrease, and the gas will get exposed to a slower energy decrease in the system due to the heat exchange between the fluid and the gas inside the accumulator. This effect will result in a slower discharge of the fluid inside the system. In Figures 5.4 to 5.6 it is observed that the maximum deviation is occurring close to the precharge pressure. One of the reasons for this large discrepancy can

be due to the fact that there in this CFD model is no physical divider between the air and the water-glycol mix. When the accumulator is close to fully discharged and the volume of fluid is close to zero a problem will arise. The gas will penetrate the fluid, and a mixture of fluid and gas will appear at the outlet of the accumulator, this will lead to inaccurate results of the simulation close to the precharge pressure. This effect will not influence the experiments, and due to this phenomena the simulations where stopped before a total penetration of gas occurs, and affects the results in negatively manner. A visualization of this phenomena is shown in Figure 6.1.

As for the average discrepancies for the three different simulations, the results obtained has a good agreement to both the analytical approach as well as the experimental study conducted by Stenhjem (2018). The model developed in STAR-CCM+ shows promising results, and is a good basis for modeling the two accumulators.

Figure 6.1: Surface visualization of gas penetrating the fluid.

6.2 Generalized Model

The different compared pressure profile with respect to time is shown in Figures 6.2, 6.4 and 6.5. In these figures the effect of changing the outlet characteristics is presented, and yields that the discharge time will be reduced significantly, but all profiles has a similar exponential decrease when discharged. By studying Figure 6.2 it can be seen that changing the ambient temperature will not affect the discharge time substantially. From Figure 6.3 the difference in discharge time is displayed, the first few seconds of discharge shows the fastest pressure drop and a very similar pressure profile for the different ambient temperatures. When the time increases, the discrepancies in the profiles will increase, and the case with the slowest discharge is the case with the highest ambient temperature. This is due to the temperature difference between the gas and the temperature of the surroundings, the larger the temperature difference, the bigger is the heat loss, which will affect the pressure drop in the system. The loss of energy due to heat transfer can be calculated by Equation (3.21), which estimates the convection in the system. When studying Figures 6.4 and 6.5 it can be seen that the discharge time is affected by the outlet restriction in a significant manner. If these figures are compared, by increasing the outlet area of the nozzle, and keeping the backpressure constant will result in profiles where the first measured pressure in the outlet pipe has a large deviation from the initial pressure. The same phenomena can be observed from Figure 6.5 where the outlet area was kept constant, but in this figure the starting pressure is not as affected as the cases where the outlet area was changed. This can be caused by the difference in restrictions in the outlet nozzle. When changing the outlet area the restriction will be more affected than by only changing the backpressure of the system, and the outlet mass flow will be higher, which will result in a greater pressure drop in the system.

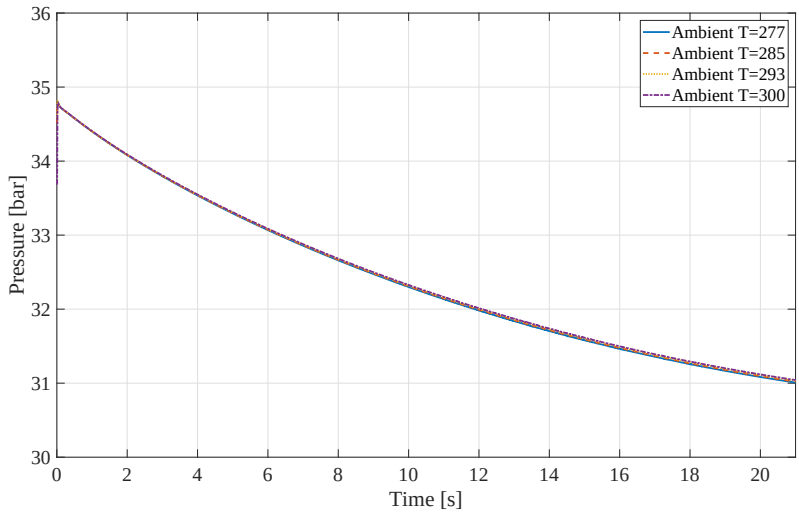

Figure 6.2: Pressure profiles for the different ambient temperature for the outlet area 12.56 mm^2.

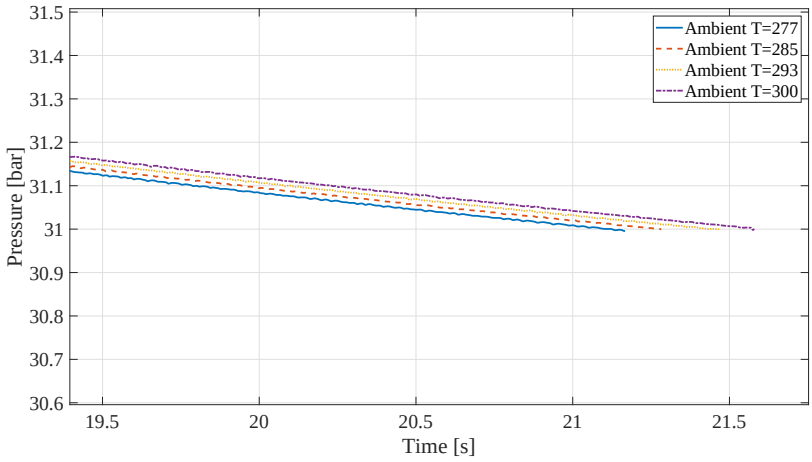

Figure 6.3: Zoom of pressure profiles at discharge end.

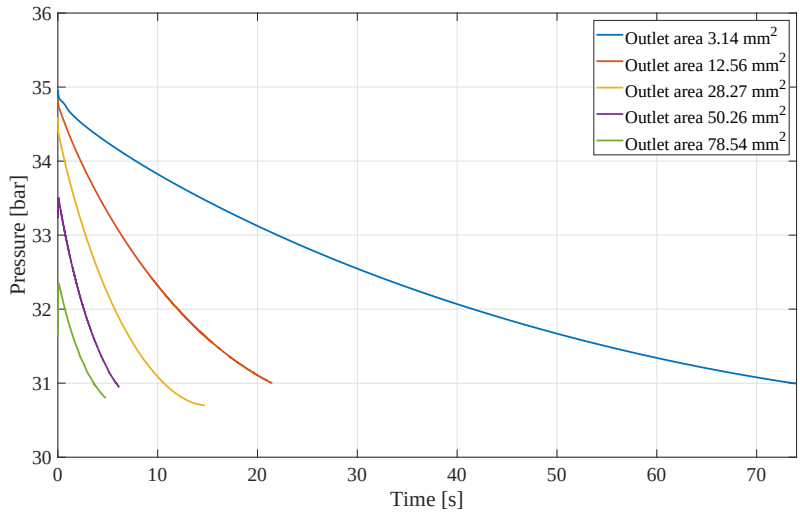

Figure 6.4: Pressure profiles for the different outlet areas.

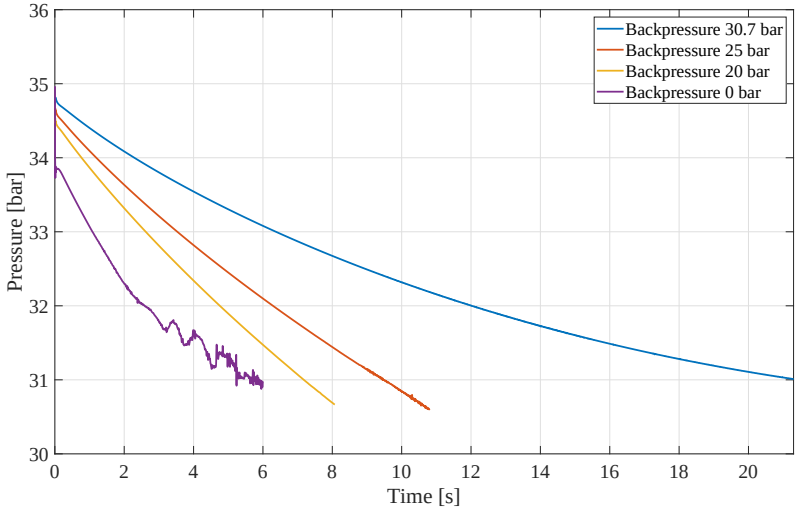

Figure 6.5: Pressure profiles for the different backpressure.

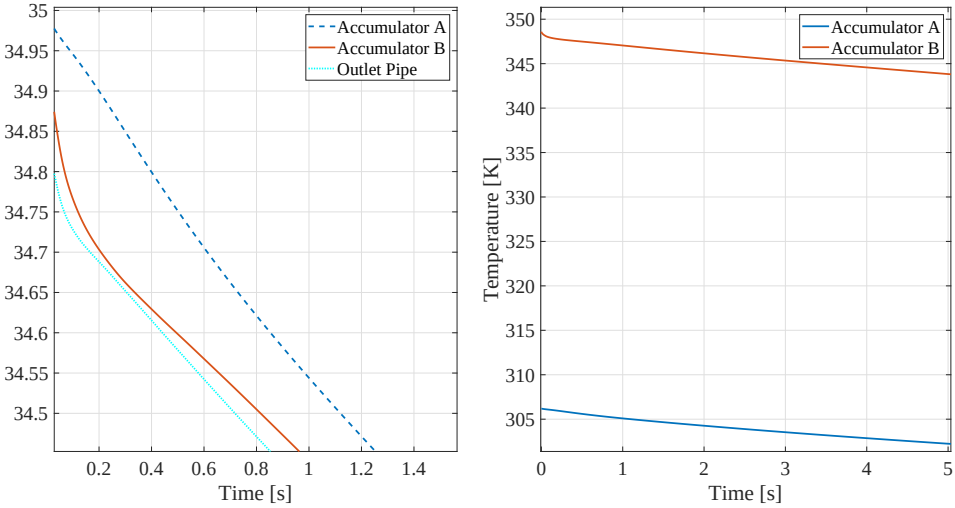

Figure 6.6: Magnified pressure and temperature profiles outlet area 12.56 mm^2 backpressure 30.7 bar and ambient T = 293K.

In Figure 6.6 a magnified presentation of the first few seconds of the base case simulation is displayed. The values of interest is the compared profiles of pressure for both accumulator A and B, and the pressure measured on the outlet pipe, as well as the temperature profiles inside the gas domain of each accumulator. This figure represents that

there in the first part of the outlet pressure profile, as well as the pressure profile in accumulator B has a rapid pressure drop before stabilizing. This pressure drop has an effect on the temperature profile in the same accumulator, as the figure displays, the temperature drops rapidly in the first 0.2 seconds which corresponds to the rapid pressure drop in this accumulator. This rapid pressure drop is caused by the flow out of accumulator B, where in the first part of discharge accumulator B will have a greater flow out of the accumulator than accumulator A. This difference in flow will result in a more rapid pressure drop in accumulator B. When considering the velocity vector field in the T-joint where the flow of accumulator A meets the flow out of accumulator B can it be noticed that the velocity out of accumulator B is larger than the flow out of A in the first part of the discharge. This deviation of velocity will result in a difference in pressure drop in the two accumulators, where accumulator B discharging faster than A, before the velocity evens out and the pressure drop will be similar for both accumulators and in the outlet pipe. The velocity vector field is shown in Figure 6.7, where the first 0.125 seconds is presented. When analyzing Figure 6.7a it is visualized that the velocity out of accumulator B is larger than for accumulator A, the velocity out of the two accumulators will even out after approximately 0.1 seconds. The results obtained from the velocity fields will indicate that there will be a more rapid pressure drop in accumulator B in the first 0.1 seconds, as can be observed from the pressure profiles presented in Figure 6.6.

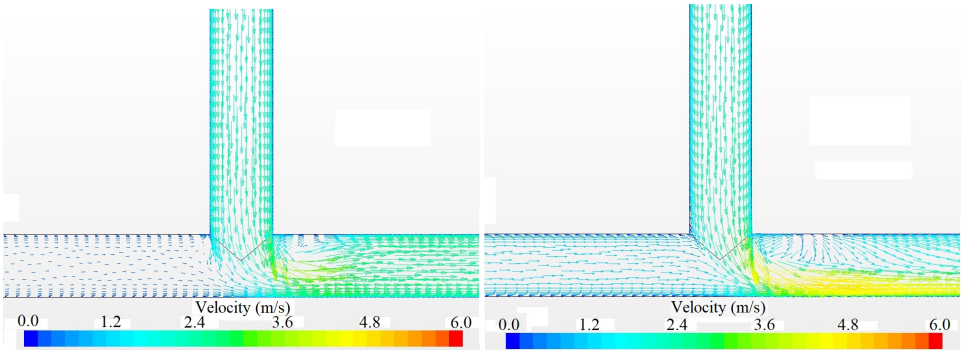

(a) Velocity vector, t=0.005 s.

(b) Velocity vector, t=0.03 s.

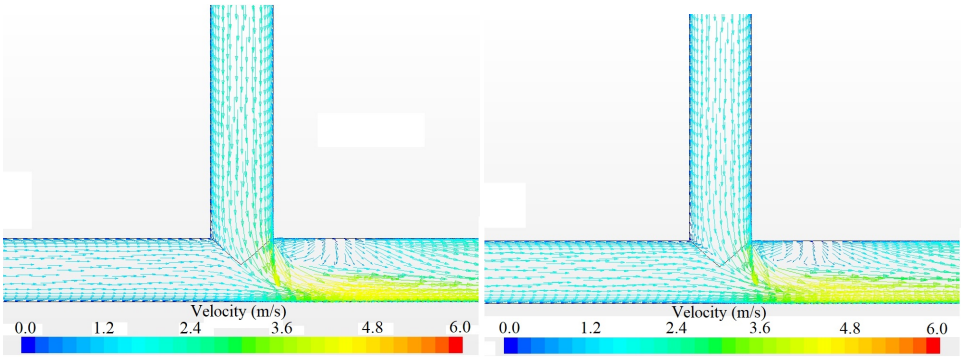

(c) Velocity vector, t=0.05 s.

(d) Velocity vector, t=0.075 s.

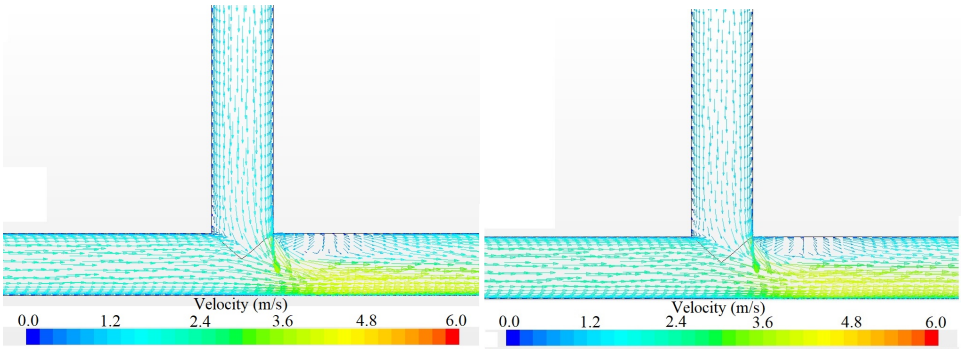

(e) Velocity vector, t=0.1 s.

(f) Velocity vector, t=0.125 s.

Figure 6.7: Velocity propagation in the meeting point of accumulator A and B.

6.3 Industrial Case

In Figure 6.8 the theoretical pressure profile for a isotherm discharge is compared to the pressure profiles for both accumulator A and B, as well as the outlet pressure. From these profiles it is displayed that the actual pressure drop inside the accumulators is faster than the theoretical approach. This is caused by the fact that the theoretical equation, shown in Equation 4.8, treats the accumulators as isotherm. When the accumulators are considered isotherm the discharge will be slower, this is due to the fact that temperature in the system will kept constant, and wont affect the pressure drop. Also when developing the isotherm equation, the system was assumed to be one accumulator with the combined volume of the system modeled in STAR-CCM+, and not a system of two accumulators placed in series. These assumption does not give the most accurate results, but it gives a indication that the system simulated acts according to the theory. Even these results, with a deviation of approximately 1.5 bar at 5 seconds is good indication that the simulations provides a good estimate for the physical system.

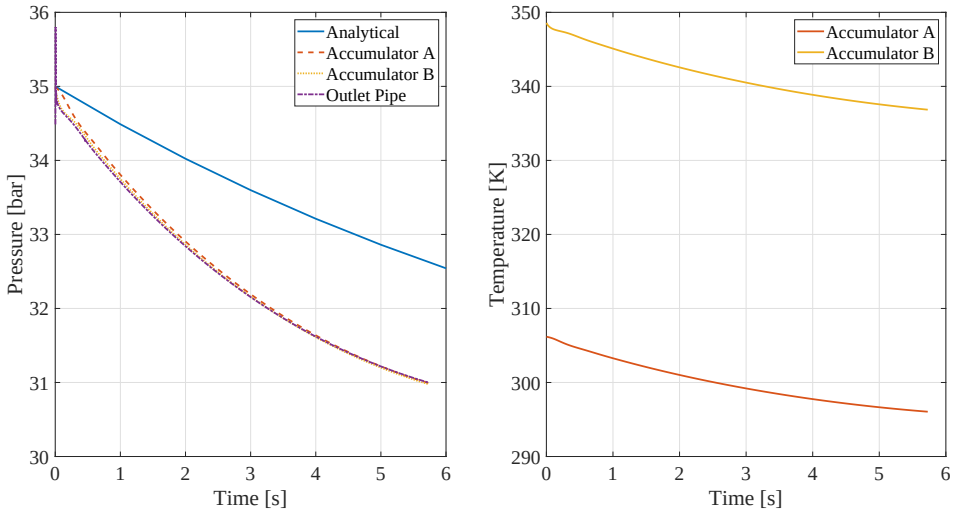

Figure 6.8: Pressure and temperature profiles for pre-charge 1, outlet are 12.56 mm^2 backpressure 30.7 bar and ambient T = 293K.

From the pressure and temperature profiles in Figure 6.8, the first part of the discharge the temperature in accumulator B has a more rapid temperature drop than accumulator A. This is the same phenomena occurring in the generalized case described above. Even when the discharge is rapid, the temperature will affect the pressure drop in a significant way, where the convention between the gas and fluid inside the accumulators will have the biggest effect on the temperature and pressure drop. As the profiles indicates, the pressure in accumulator A is a bit higher than the pressure in both accumulator B and the outlet measuring point just before the nozzle. This deviation is grater in the beginning of the discharge cycle, before the pressures in all three places evens out close to fully discharged.

This difference in pressure is caused by the velocity of fluid exiting accumulator B, which is higher then the velocity of fluid out of accumulator A.

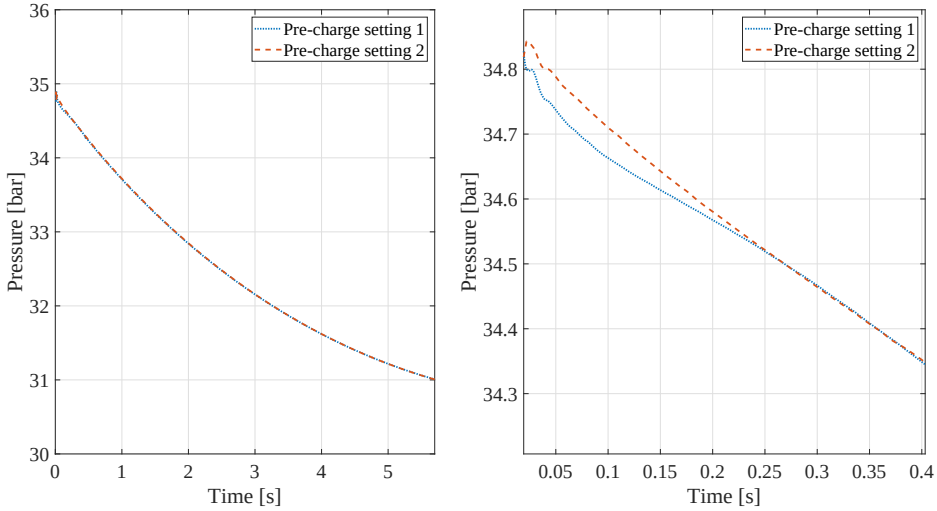

Figure 6.9: Comparison of the different pre-charge settings with backpressure of 30.7 bar, right figure is a magnified representation of the pressure drop.

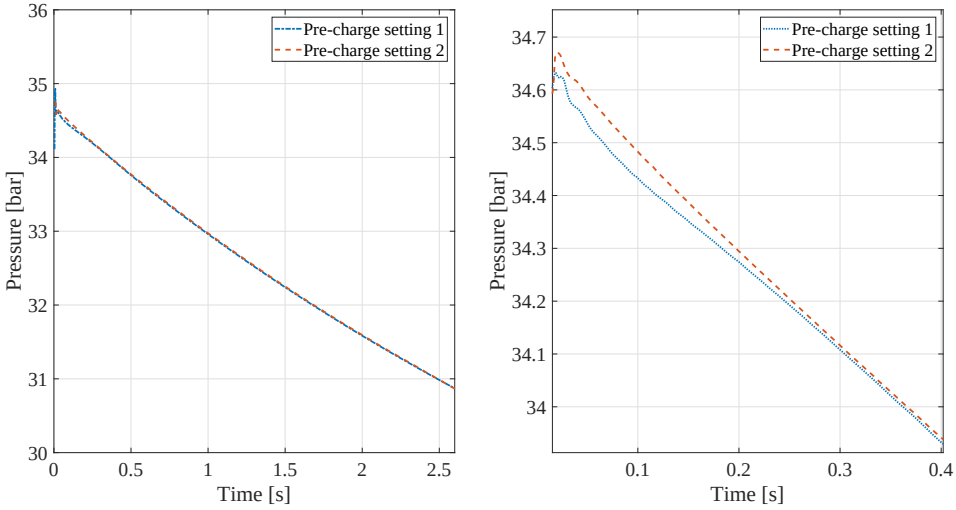

Figure 6.10: Comparison of the different pre-charge settings with backpressure of 25 bar, right figure is a magnified representation of the pressure drop.

Figures 6.9 to 6.11 compares the pressure profiles in measuring point in the outlet pipe when the pre-charge order is changed. Similar for all three different backpressures is that the pre-charge setting 1 has a more rapid pressure drop in the first part of discharge, where pre-charge setting 2 has a more constant pressure decrease. When evaluation the discharge of the cases with pre-charge setting 2, the pressure drop is more stable and can give a more predicted flow out of the system. This observation is very interesting, these results can indicate that the convection between the accumulators and the surroundings wont have a significant impact on the the discharge of the system, as also observed in Irizar (2015). By changing the pre-charge setting the case studied, the system will provide a more constant and predicted flow to the multiphase pump located on the seabed.

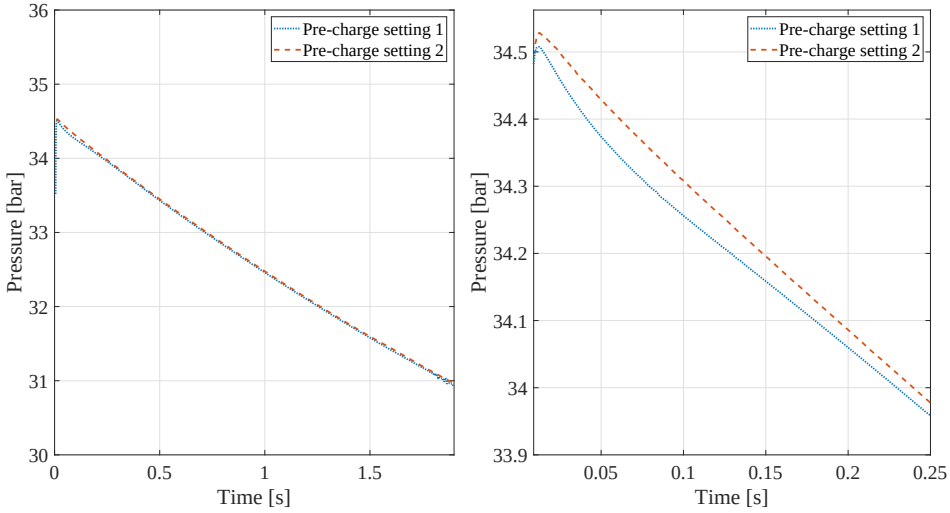

Figure 6.11: Comparison of the different pre-charge settings with backpressure of 20 bar, right figure is a magnified representation of the pressure drop.

When evaluation the pressure drop in the first 0.4 seconds of the discharge for the case with a backpressure of 30.7 bar for the two different pre-charge settings, is it visualized that there is a smaller deviation between the pressures in accumulator A and B where the pre-charge had setting 2. From Figure 6.12 a magnified representation of the first 0.4 seconds is shown for the two different pre-charge settings. In Figure 6.12a the pressure profiles when pre-charge setting 1 is applied is presented, from this figure it can be seen that the deviation between the accumulator with the highest pre-charge pressure has a more constant pressure drop than the accumulator with the lowest pre-charge pressure. The discrepancies between the two pressure profiles at 0.1 seconds is approximately 0.2 bar. When evaluation the same case with different pre-charge order, as visualized in Figure 6.12b the discrepancies between the pressure profiles in accumulator A and B is significantly lower than for the for the first pre-charge setting. The figure yields a maximum discrepancies of only 0.03 bar at time equal 0.04 seconds. When comparing these profiles it can be seen that changing the pre-charge order the pressure profile will act more stable which will result in a more

predicted flow out of the system. The profiles indicates that the flow out of the accumulator placed closest to the outlet nozzle will have a higher velocity profile in the first part of the discharge cycle, but when the pre-charge order is set to setting 2 the velocity profiles equalizes faster and the two accumulators together with the pressure just before the nozzle will yield a more stable flow pattern.

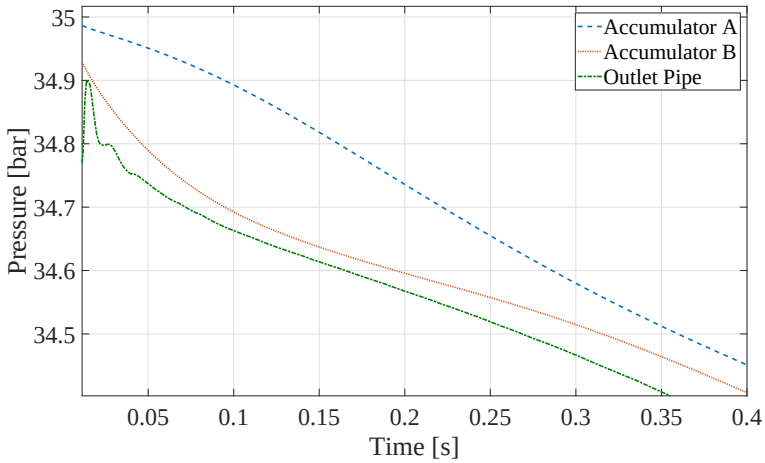

(a) Magnified representation of the first part of discharge with backpressure 30.7 bar and pre-charge setting 1.

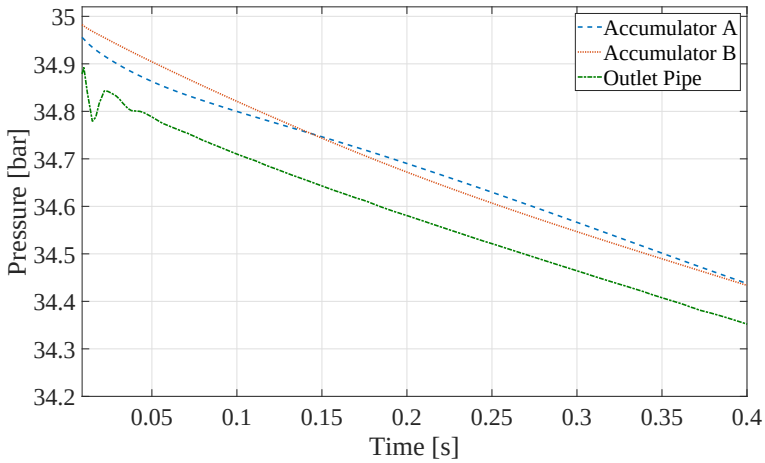

(b) Magnified representation of the first part of discharge with backpressure 30.7 bar and pre-charge setting 2.

Figure 6.12: Magnefied representation of the first part of discharge for the different pre-charge settings.

6.4 Uncertainties

When constructing the models presented in this thesis there were made some simplifications in both the geometry, as well as some physical models selected. If considering the geometry modeled there is not implemented a piston inside the accumulators due to the complexity of the 3D modeling as well as the mesh construction. When these simplifications were made, some problems arise when the accumulates was close to empty, and the fluid level is low the gas will penetrate the fluid and flow in the middle of the pipe affect the measured values obtained. The geometrical models constructed was also modeled just from the fluid volume, and does not consist of the real geometry of the different accumulators, this simplification will affect the thermodynamics in the system. In the piston accumulators the piston friction was not taken into account when computing the cases described in this thesis, this friction force will have an effect on the discharge of accumulators. When selecting the physical models for the different cases, they all was based on a model constructed in a pre-project conducted by Hiis and Stenhjem (2017), which is based on the Reynolds average Navier Stokes model with multi-phase flow. When these physical models are chosen there is not possible to model the gas as real, which indicates that the models conducted in this thesis treats the gas as ideal, this assumption can lead to some deviations from reality in the results. When comparing the results of the single bladder accumulator to the experiments and the theoretical approach, the result is satisfactory and the discrepancies are very low.

STAR-CCM+ is a complex software with numerous variables to consider for the physics, mesh generation, and solver settings. Even though the residuals observed in these simulations were adequate, some errors in the setup could be an error source, or some choices made which could not be optimal for the cases studied, due to the lack of experience in the program.

Chapter 7

Conclusion

The numerical study of three different cases of hydraulic accumulators has been preformed, the CFD model was developed with use of the commercial software STAR-CCM+. The first case studied is a single bladder-type accumulator discharge through three different outlet areas, the physical model made is validated by an experimental study as well as a theoretical approach. The average discrepancies obtained was below 12.56% for all cases modeled, these results yields a high level of agreement to the various validation points, which leads to significant credibility of the physical model developed. This model is then to be adapted to the following cases in this study.

The second case studies a set of two accumulators in series with different pre-charge pressures, and equal charge pressures. The results obtained indicates that the discharge of the different accumulators will result in different pressure profiles. Where the accumulator with the lowest pre-charge has a more rapid pressure drop than the accumulator with the highest pre-charge, which is due to the flow pattern out of the different accumulators. The case was studied by changing the ambient temperature, outlet area of the nozzle, and by changing the pressure on the nozzle outlet. Due to the fast discharge time, the change of ambient temperature will not have significant effect on the discharge. By changing the outlet area of nozzle, the discharge of the system was substantially changed due to the difference in restriction in the outlet nozzle. This effect was obtained by changing the backpressure as well, but not to the same extent.

The third case studied is similar to the second case, but the accumulator volumes is smaller. In this case the effect of changing the pre-charge order was studied together with the change of backpressure of the system. The results obtained from this study shows that changing the pre-charge order will provide a more constant pressure delivery without a rapid pressure drop in the system. This will result in a more stable and predictable flow out of the hydraulic system studied. Even when changing the restrictions in the outlet nozzle, the results shows a more stable flow out of the system, with similar pressure profiles.

Future work

For the CFD modeling, there would be interesting to model a more realistic geometry of the accumulators, where the piston was implemented and accumulator body was identical to the actual accumulators, and not only the fluid volume. The results from the realistic model should be compared to the simplified model developed in this thesis to identify the deviations, and see the impact of the differences in the models. It would also be of interest to change the physical model selected, and implemented the piston friction as well as treating the gas as real, and not only ideal. To be able to identify the impact of these simplifications which was made when the model in study was developed.

Another point of interest would be changing and analyzing different pre-charge pressures for the accumulators to find the optimal pre-charge that will yield the most desired flow pattern and pressure profiles in the system. And compare the results with a model that accounts for the full charge and discharge cycle of the systems to be sure to obtain the correct pressure and temperature in the different accumulators.

Bibliography

Anderson, J. D., 1995. Computational Fluid Dynamics, The Basics with Applications. McGraw-Hill, Inc.

Armstrong-Hélouvry, B., Dupont, P., De Wit, C. C., 1994. A survey of models, analysis tools and compensation methods for the control of machines with friction. Automatica 30 (7), 1083–1138.

Ashton, B. N., Apr. 20 1948. Piston type accumulator. US Patent 2,440,065.

Balakin, B. V., Kuzmenkov, D. M., Kutsenko, K., Maslov, Y. A., Saparbaeva, N. A., Kharitonov, V. S., 2017. Computational study of two-phase flow morphology in a nozzle.

Brautaste, K., 2013. Innforing i olje hydraulikk. Gyldendal Norsk Forlag.

Gibson, J., Pierce, M., 2010. Remnants of early hydraulic power systems. Australian Journal of Multi-disciplinary Engineering 8 (1), 33–45.

Haq, N. U., 2010. Design and modelling of a piston accumulator for rock drill and its fatigue strength. In: Degree Project, Department of Management and Engineering at Lindkopings University, Sweeden. pp. 34–35.

Hiis, E., Stenhjem, M. A., 2017. Analysis of accumulator discharge.

Hirt, C. W., Nichols, B. D., 1981. Volume of fluid (vof) method for the dynamics of free boundaries. Journal of Computational Physics 39 (1), 201–225.

Irizar, V., 2015. Advanced modeling and verification of an hydraulic accumulator.

Jean, M., Oct. 19 1943. Storage device. US Patent 2,331,921.

Kjolle, A., 1989. Oljehydraulikk. Tapir.

Liseikin, V. D., 2010. Grid Generation Methods. Scientific Computation. Springer Netherlands, Dordrecht.

Mathworks, 2017. Translation friction.
URL `https://se.mathworks.com/help/physmod/simscape/ref/translationalfriction.html`

Mitsubishi Heavy Industries, L., 2011. Cfd analysis for advanced accumulator.

NOAA, 2018. Great lakes coastal forecasting system: Next generation.
URL https://www.glerl.noaa.gov/res/Programs/ipemf/GLCFS_nextgen.html

Olsen, N. R. B., 2007. Numerical modelling and hydraulics. The Norvegian University of Science and Technology, Trondheim.

Siemens, 2017. STAR-CCM+® Documentation, Version 12.04.

Stenhjem, M. A., 2018. Experimental study of hydraulic accumulator discharge.

Thibaut, E., Meyer, E., Bibet, P. J., 2010. Use of liquid filled motor for subsea pump applications. In: PCIC Europe 2010. pp. 1–8.

Wang, W., Zhuan, R., 2009. Numerical simulation of micro scale flowing and boiling. Frontiers of Energy and Power Engineering in China 3 (4), 396.

Appendix

Appendix A

Calculation

A.1 Two accumulators

Gas volume of the accumulators are calculated by Equation 4.1 and for generalized case the accumulator with pre-charge of 19 bar has a gas volume calculated like:

$$V_1 = \left(\frac{19bar}{35bar}\right)^{\frac{1}{1.4}} \times 40l = 25.85l \tag{A.1}$$

Charge volume of gas in generalized accumulator with pre-charge of 30 bar is calculated as follows:

$$V_1 = \left(\frac{30bar}{35bar}\right)^{\frac{1}{1.4}} \times 40l = 35.83l \tag{A.2}$$

For the industrial case, the gas volumes for the two different pre-charges is calculated and shown below, first the volume where the pre-charge is 19 bar, then the gas volume of pre-charge 30:

$$V_1 = \left(\frac{19bar}{35bar}\right)^{\frac{1}{1.4}} \times 10l = 6.46l \tag{A.3}$$

$$V_1 = \left(\frac{30bar}{35bar}\right)^{\frac{1}{1.4}} \times 10l = 8.96l \tag{A.4}$$

The corresponding charge temperatures is calculated by Equation 4.2, the charge temperature where the pre-charge is 19 bar is:

$$T_1 = 293K \times \left(\frac{10l}{6.46l}\right)^{0.4} = 348.6K \tag{A.5}$$

The charge temperature when pre-charged with 30 bar is calculated as:

$$T_1 = 293K \times \left(\frac{10l}{8.96l}\right)^{0.4} = 306.2K \tag{A.6}$$

The total mass of gas used in the theoretical accumulator is calculated by Equation 4.9 as follows:

$$m_{tot} = \frac{2PVM}{RT} = \frac{2 \times 19 \times 10^5 Pa \times 0.01 m^3 \times 28.0174 \times 10^{-3} kg/mol}{8.314 kgm^2/molKs^2 \times 293K} = 0.437\ kg \tag{A.7}$$

The mass m_{tot} is then used to calculate the total volume of gas in the theoretical accumulator:

$$v_{theoretical} = \frac{m_{tot}TR}{PM} = \frac{0.437kg \times 293K \times 8.314 kgm^2/molKs^2 \times}{19 \times 10^5 Pa \times 28.0174 \times 10^{-3} kg/mol} = 0.12667\ m^3 \tag{A.8}$$

A.1.1 Matlab Code

```
clc
clear
syms p
C = (atan(sqrt(3500000-3070000)/sqrt(3070000)))
    /3070000^1.5+sqrt(3500000-3070000)/(3500000.*3070000);
p_ch = 3500000;
A = pi.*0.002^2;
mu = 0.49;
rho = 869;
p_0 = 3070000;
v = 0.0126666857;
B = A.*mu.*sqrt(2/rho);

p_losn(30,1) = 0;
for i = 1:30
    losning = solve((atan(sqrt(p-p_0)/sqrt(p_0)))/p_0^1.5+
        sqrt(p-p_0)/(p.*p_0)==-(B.*i)/(p_ch.*v)+ C,p);
    p_losn(i)= losning;
end
```

Appendix B

Additional results

B.1 Bladder-type accumulator

Table B.1 shows the values used to compare the dimensionless results with the other cases conducted, in the table, simulations conducted in STAR-CCM+ is marked with *CFD*, and experiments conducted by Stenhjem (2018) is marked with *Experiment*, and obtained from Stenhjem (2018). This comparison is shown in Figure 5.7.

Outlet area	φ	tan(φ)	Re	
2.53 mm^2	10.5	0.19	20526	*CFD*
15.4 mm^2	11	0.19	57864	*CFD*
38.1 mm^2	15	0.27	106487	*CFD*
2.53 mm^2	7.5	0.13	20526	*Experiment*
15.4 mm^2	13.5	0.24	57864	*Experiment*
38.1 mm^2	17	0.31	106487	*Experiment*

Table B.1: The three simulations conducted together with the angle φ, tan(φ) and the corresponding Reynolds number.

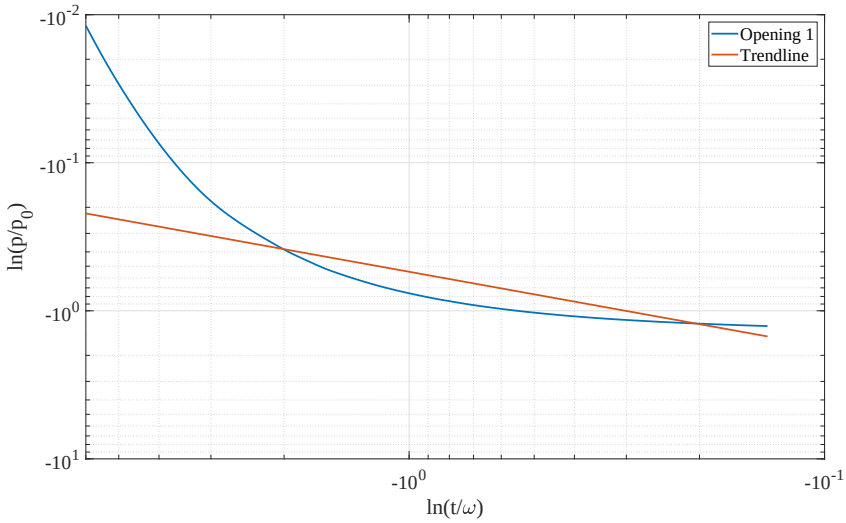

Figure B.1: Dimensionless plot for opening area 1.

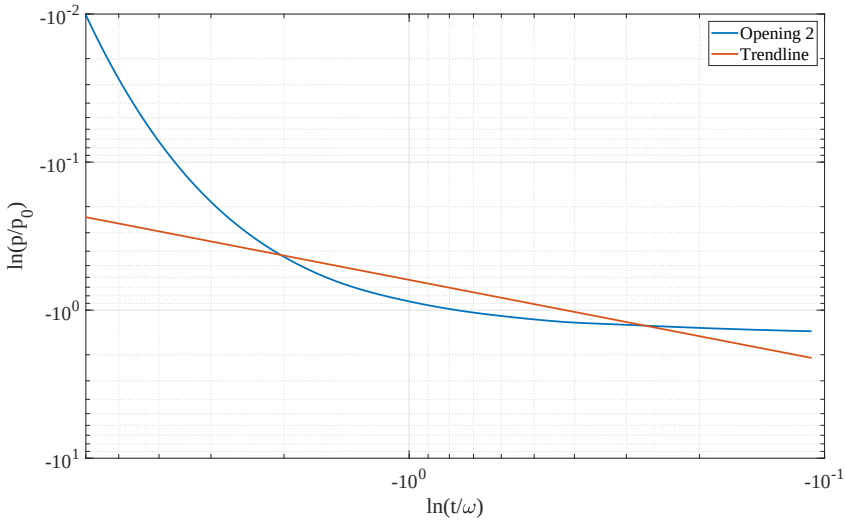

Figure B.2: Dimensionless plot for opening area 2.

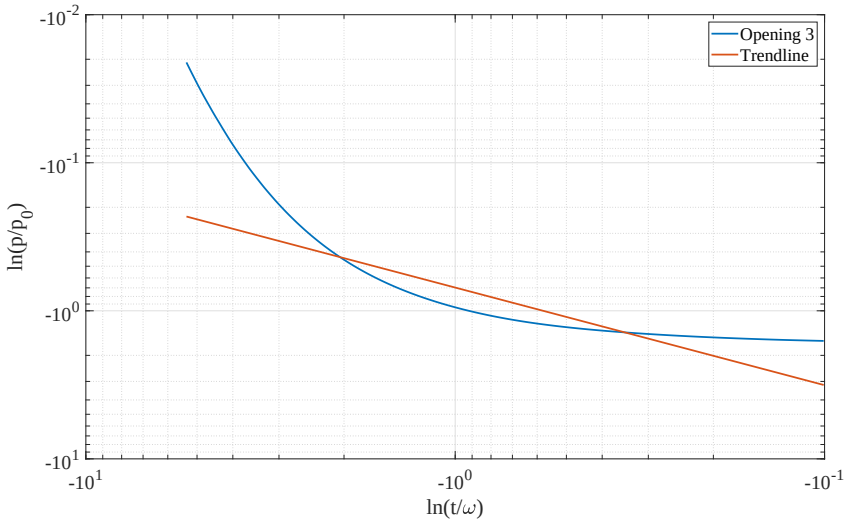

Figure B.3: Dimensionless plot for opening area 3.

B.2 Generalized Model

From Figure B.4 shows the base case simulation profiles for both pressure and temperature.

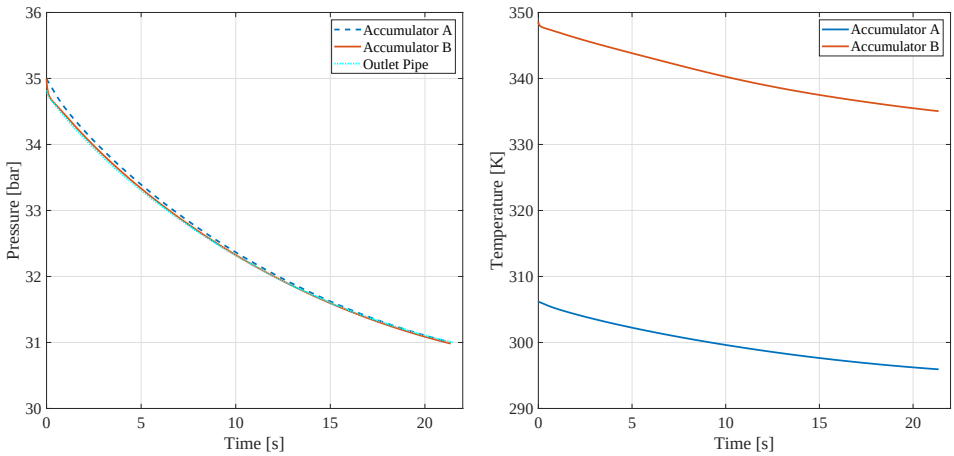

Figure B.4: Pressure and temperature profiles outlet area 12.56 mm^2 backpressure 30.7 bar and ambient T = 293K

In Figure B.5 the results of pressure and temperature profiles for outlet area of 12.56 mm^2, backpressure of 30.7 bar and an ambient temperature of 4°C is shown.

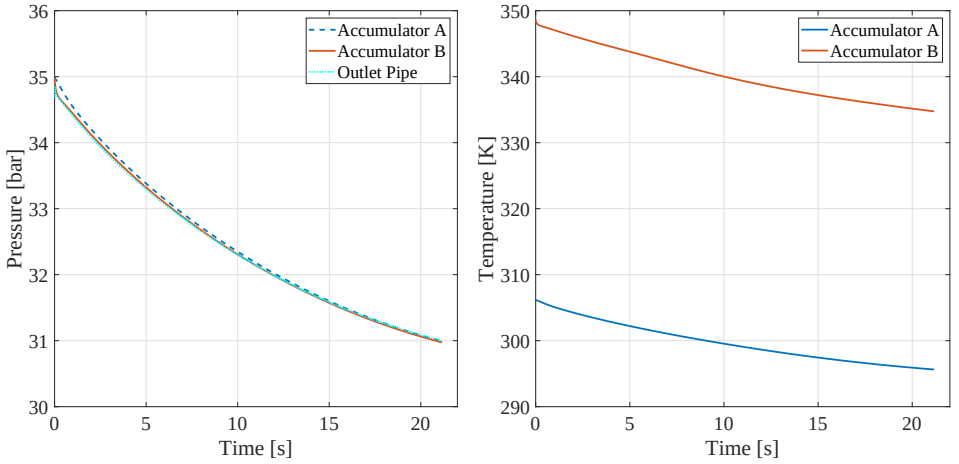

Figure B.5: Pressure and temperature profiles for outlet area 12.56 mm^2 backpressure 30.7 bar and ambient T = 277K

Figure B.6 shows the discharge profiles for simulation where the outlet area is 12.56 mm^2, backpressure is 30.7 bar, and the ambient temperature is 12°C.

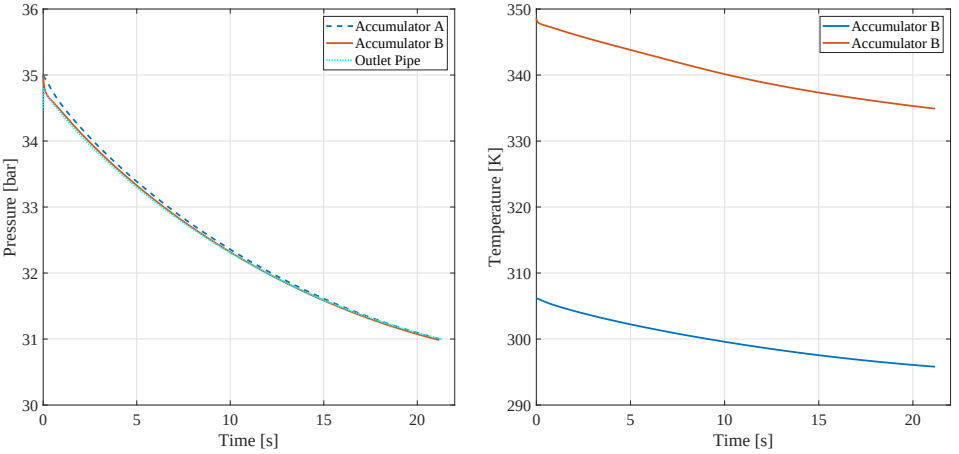

Figure B.6: Pressure and temperature profiles for outlet area 12.56 mm^2 backpressure 30.7 bar and ambient T = 285K

Figure B.7 shows the profiles of pressure and temperature where the outlet area is 12.56 mm^2, backpressure is 30.7 bar, and the ambient temperature is 27°C.

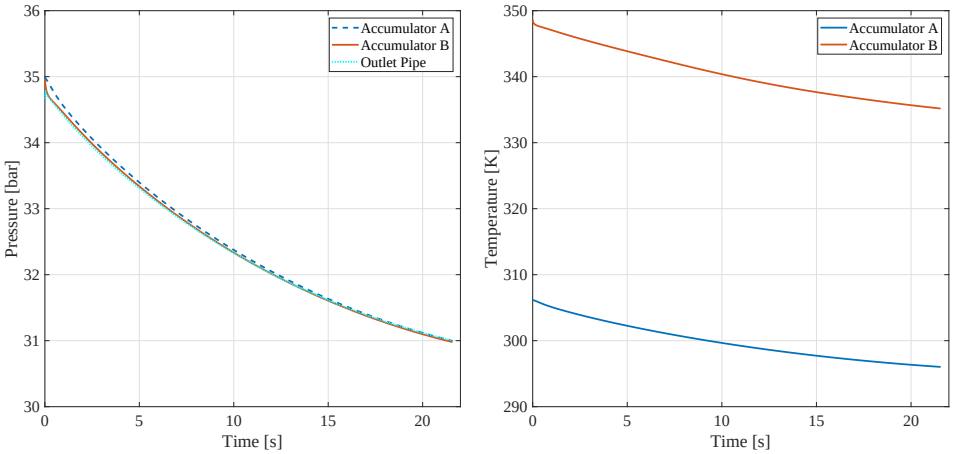

Figure B.7: Pressure and temperature profiles for outlet area 12.56 mm^2 backpressure 30.7 bar and ambient T = 300K

Figure B.8 shows the results of discharging the accumulators through an outlet area of 12.56 mm^2 with a backpressure of 25 bar and ambient temperature of 20°C.

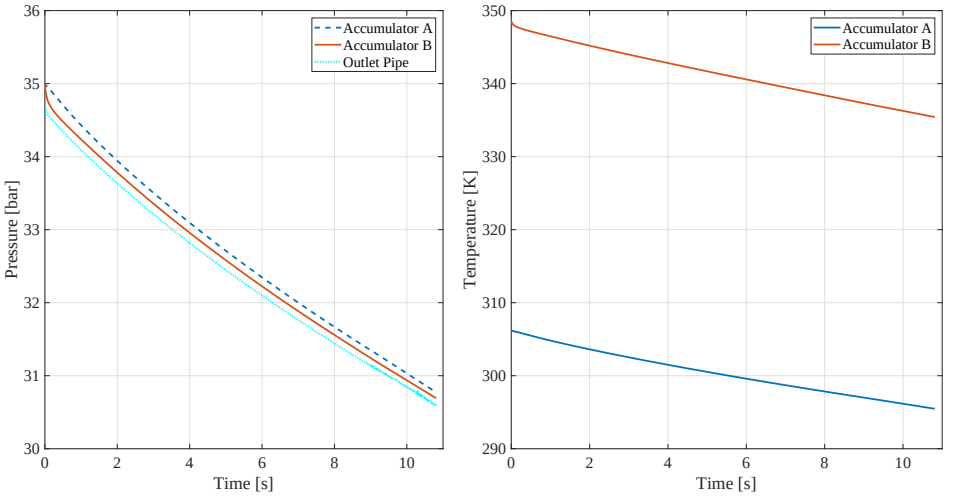

Figure B.8: Pressure and temperature profiles for outlet area 12.56 mm^2 backpressure 25 bar and ambient T = 293K

The pressure and temperature profiles for discharge of outlet 12.56 mm^2 with ambient temperature of 20°C and a backpressure of 20 bar is shown in Figure B.9.

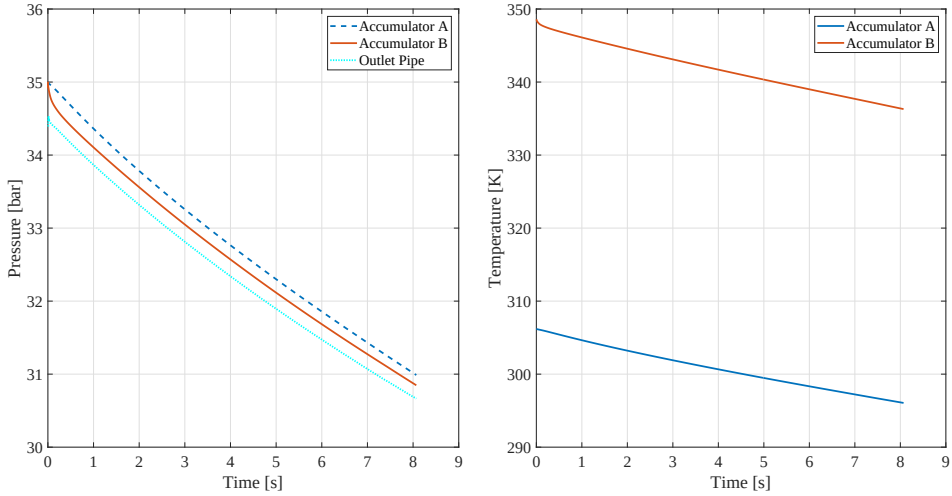

Figure B.9: Pressure and temperature profiles for outlet area 12.56 mm^2 backpressure 20 bar and ambient T = 293K

The profiles shown in Figure B.10 represents the pressure and temperature profiles where the outlet area is 12.56 mm^2, the ambient temperature is 20°C, and the accumulators is discharging to atmosphere.

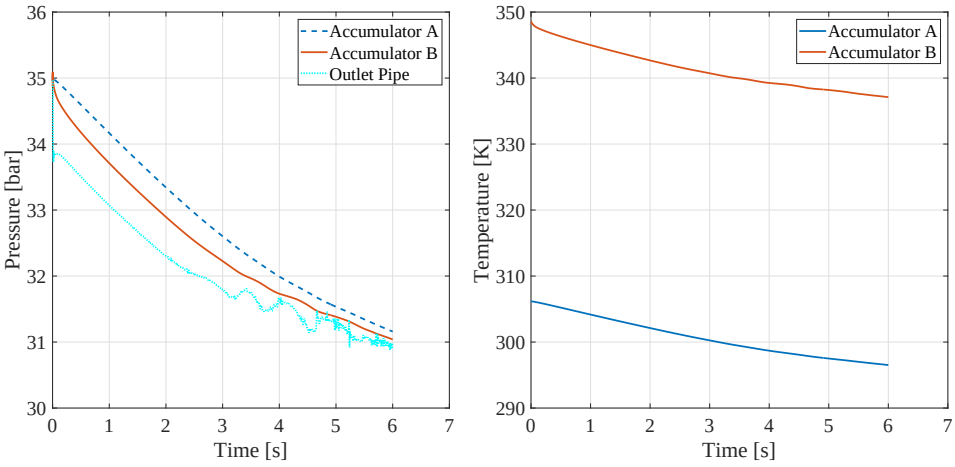

Figure B.10: Pressure and temperature profiles for outlet area 12.56 mm^2 backpressure 0 bar and ambient T = 293K

The results shown in Figure B.11 represent the discharge through the smallest outlet area of 3.14 mm^2 with a backpressure of 30.7 bar, and the ambient temperature of 20°C.

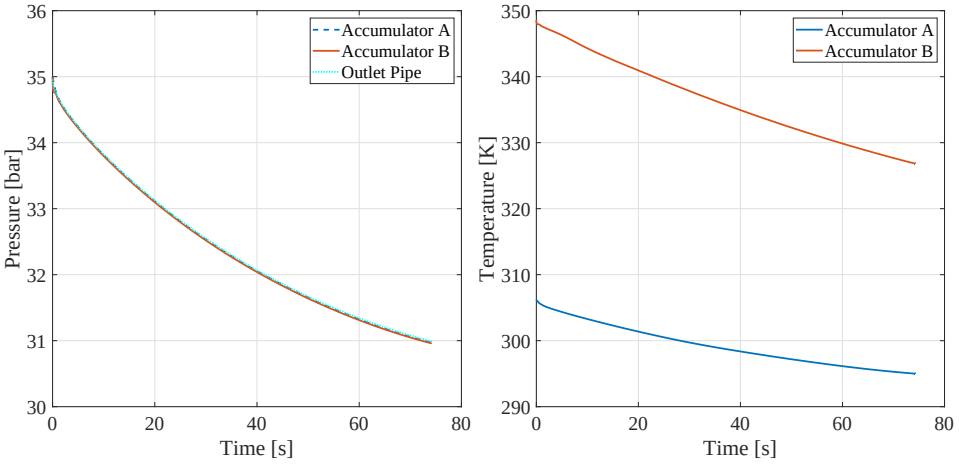

Figure B.11: Pressure and temperature profiles for outlet area 3.14 mm^2 backpressure 30.7 bar and ambient T = 293K

Below the Figure B.12 shows the pressure and temperature profiles for the simulation where the outlet area is 28.27 mm^2, backpressure is 30.7 bar, and the ambient temperature is 20°C.

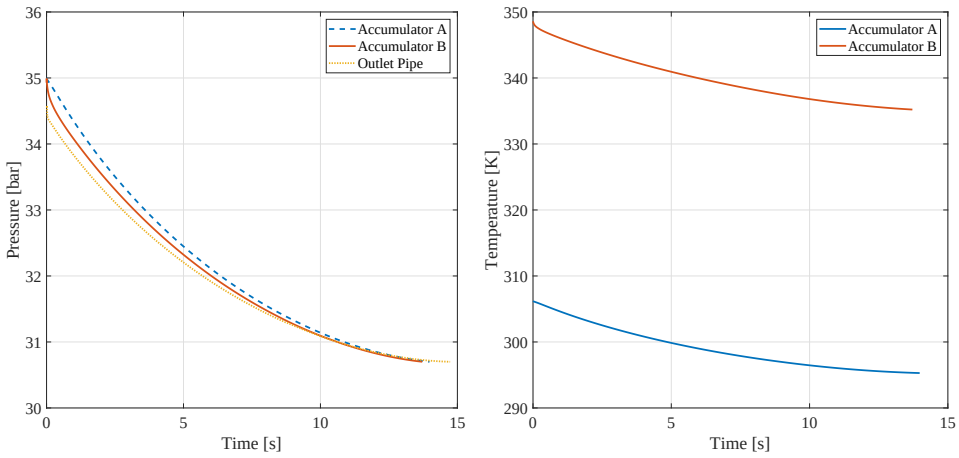

Figure B.12: Pressure and temperature profiles for outlet area 28.27 mm^2 backpressure 30.7 bar and ambient T = 293K

The results of the simulation done for discharging through the outlet area of 50.26 mm^2, with an ambient temperature of 20°C, and with a backpressure of 30.7 bar.

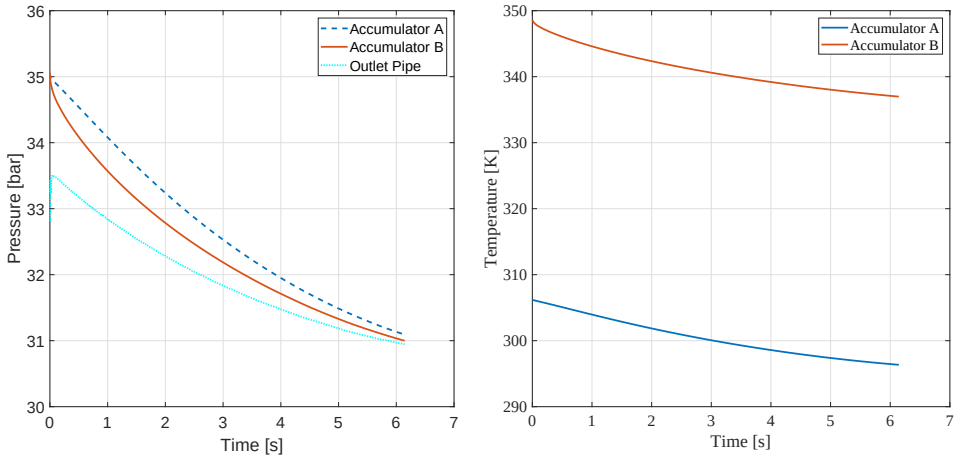

Figure B.13: Pressure and temperature profiles for outlet area 50.26 mm^2 backpressure 30.7 bar and ambient T = 293K

The results of the simulation done for discharging through the outlet area of 78.54 mm^2, with an ambient temperature of 20°C, and with a backpressure of 30.7 bar.

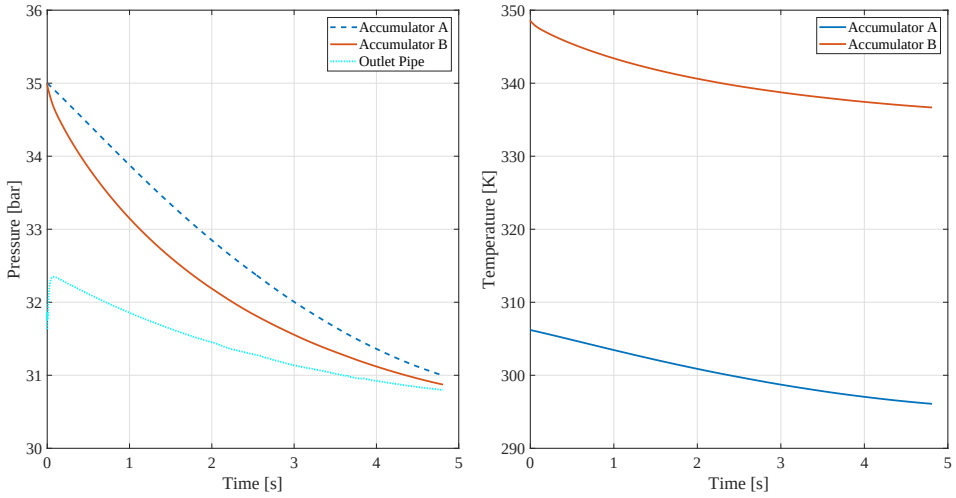

Figure B.14: Pressure and temperature profiles for outlet area 78.54 mm^2 backpressure 30.7 bar and ambient T = 293K

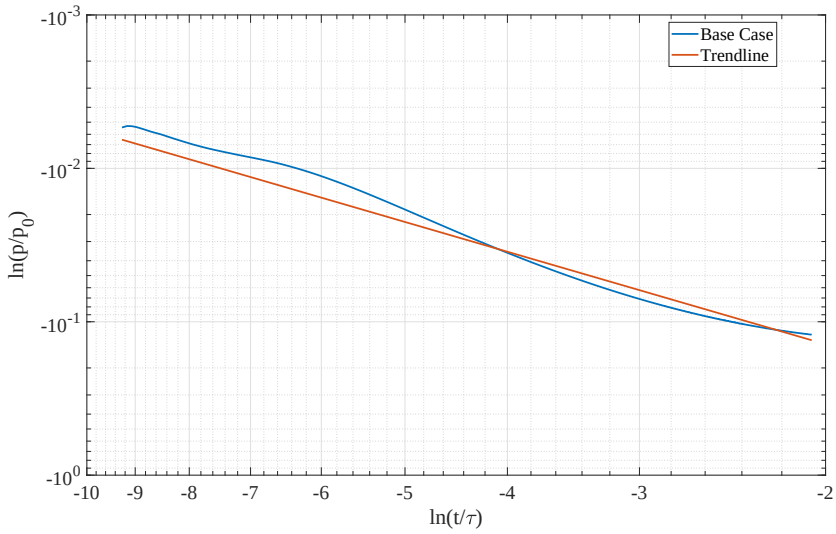

Figure B.15: Dimensionless plot for outlet area 12.56 mm^2 backpressure 30.7 bar and ambient T = 293K

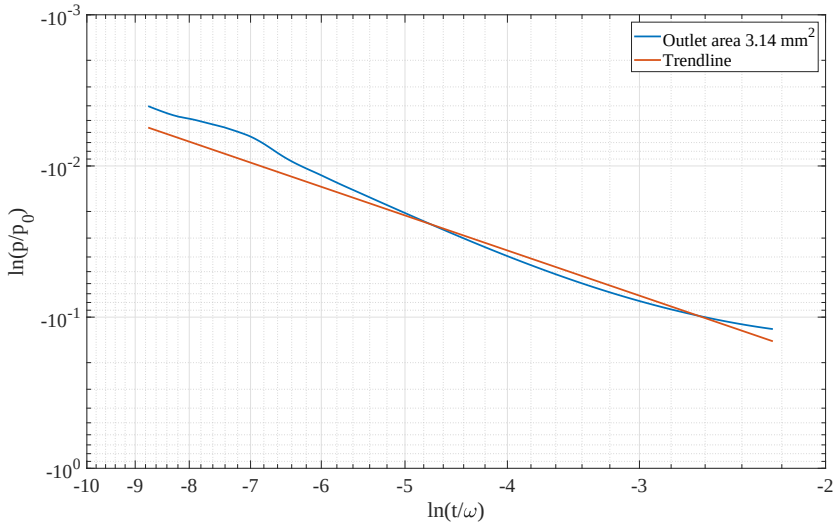

Figure B.16: Dimensionless plot for outlet area 3.14 mm^2 backpressure 30.7 bar and ambient T = 293K

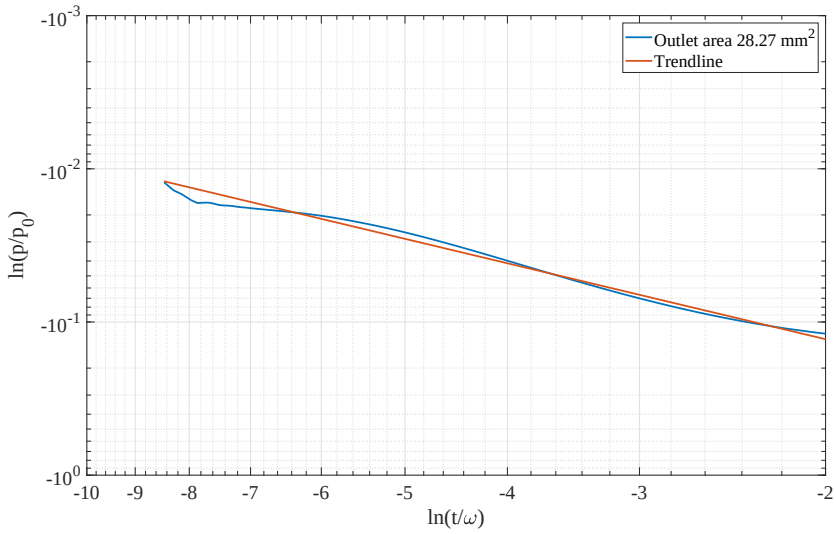

Figure B.17: Dimensionless plot for outlet area 28.27 mm^2 backpressure 30.7 bar and ambient T = 293K

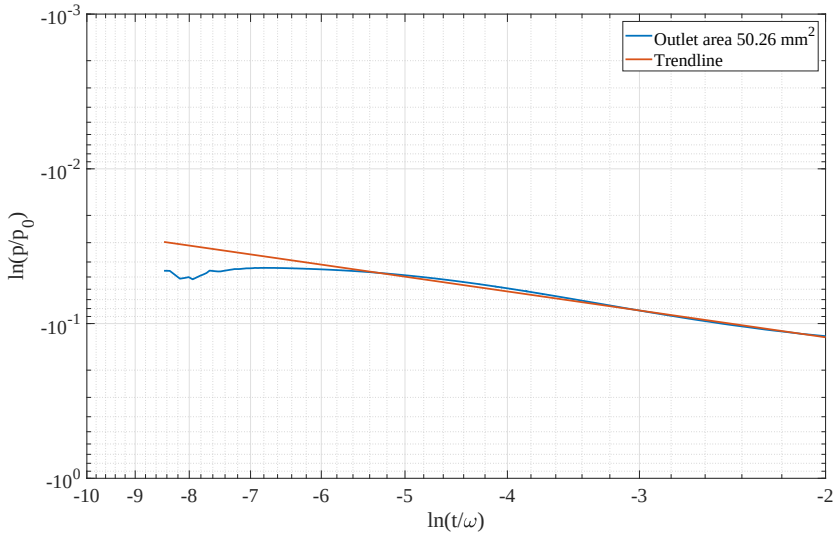

Figure B.18: Dimensionless plot for outlet area 50.26 mm^2 backpressure 30.7 bar and ambient T = 293K

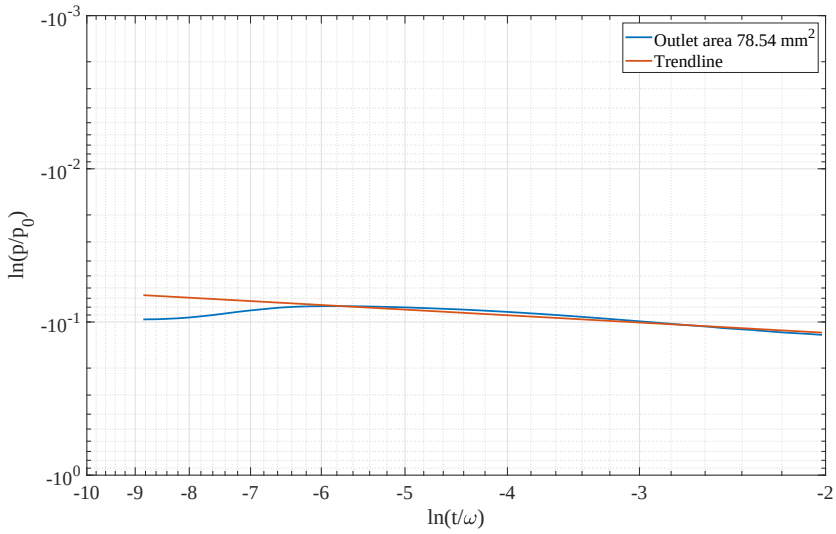

Figure B.19: Dimensionless plot for outlet area 78.54 mm^2 backpressure 30.7 bar and ambient T = 293K

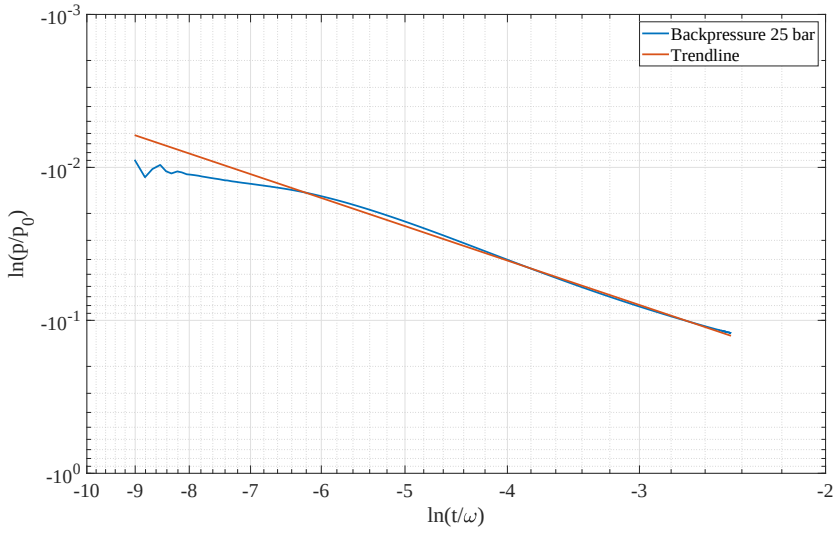

Figure B.20: Dimensionless plot for outlet area 12.56 mm^2 backpressure 25 bar and ambient T = 293K

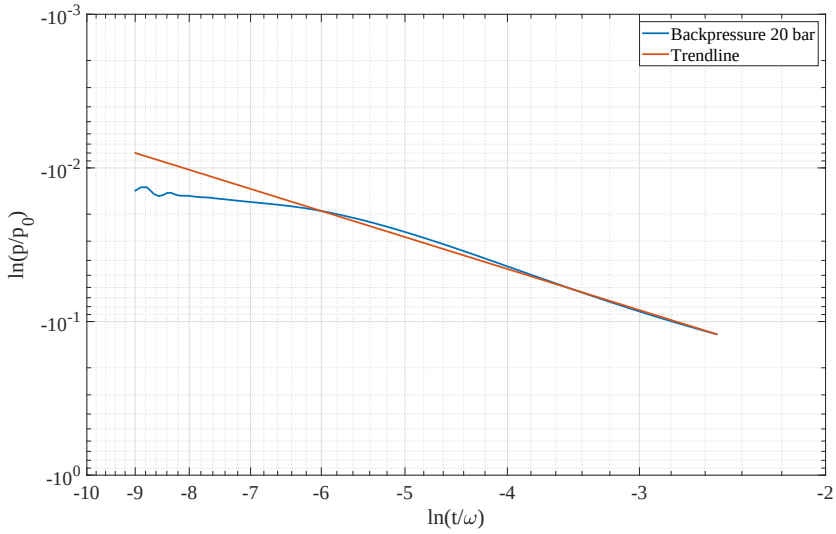

Figure B.21: Dimensionless plot for outlet area 12.56 mm^2 backpressure 20 bar and ambient T = 293K

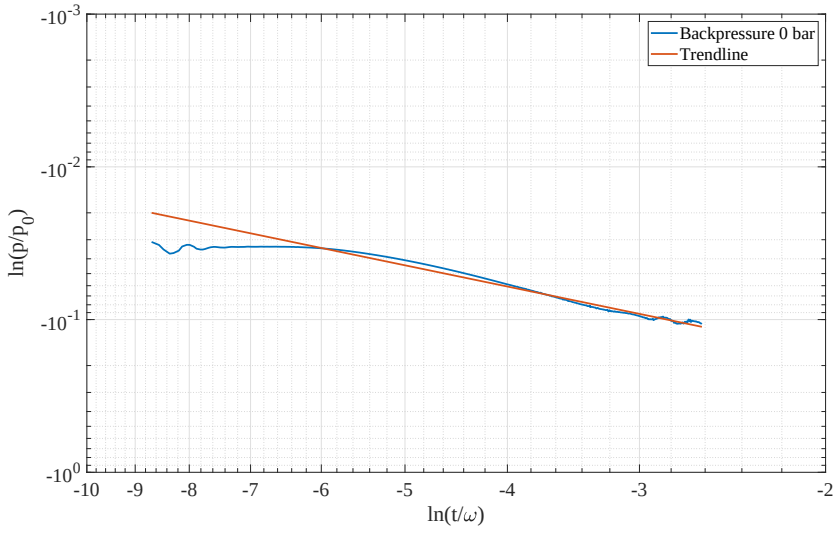

Figure B.22: Dimensionless plot for outlet area 12.56 mm^2 backpressure 0 bar and ambient T = 293K

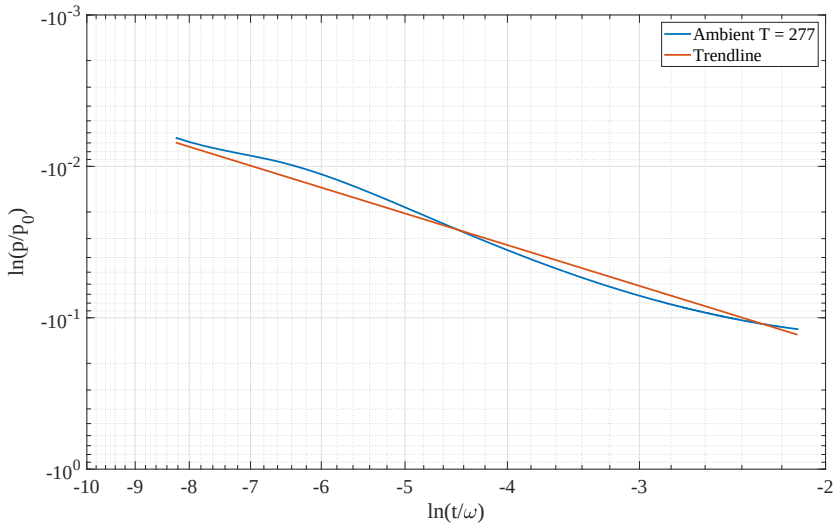

Figure B.23: Dimensionless plot for outlet area 12.56 mm^2 backpressure 30.7 bar and ambient T = 277K

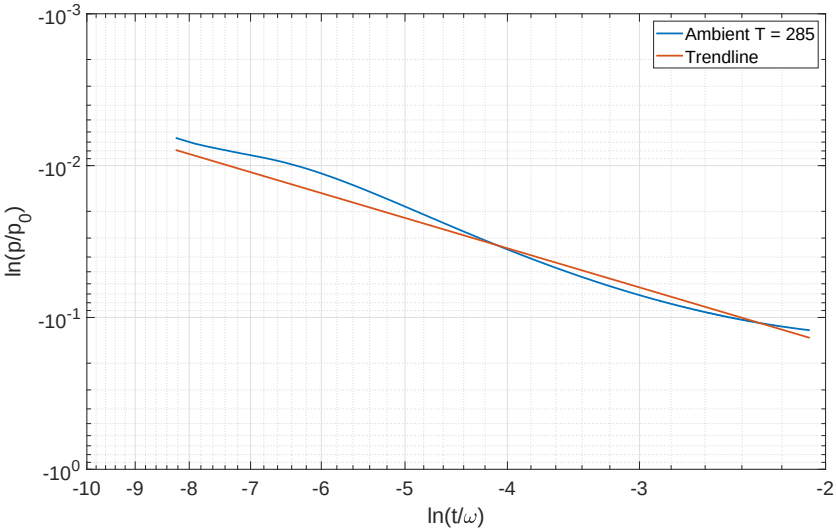

Figure B.24: Dimensionless plot for outlet area 12.56 mm^2 backpressure 30.7 bar and ambient T = 285K

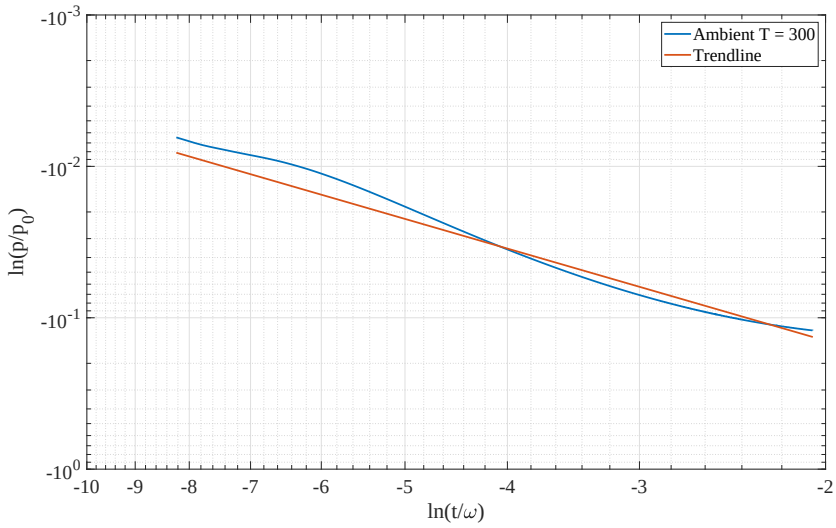

Figure B.25: Dimensionless plot for outlet area 12.56 mm^2 backpressure 30.7 bar and ambient T = 300K

B.3 Industrial model

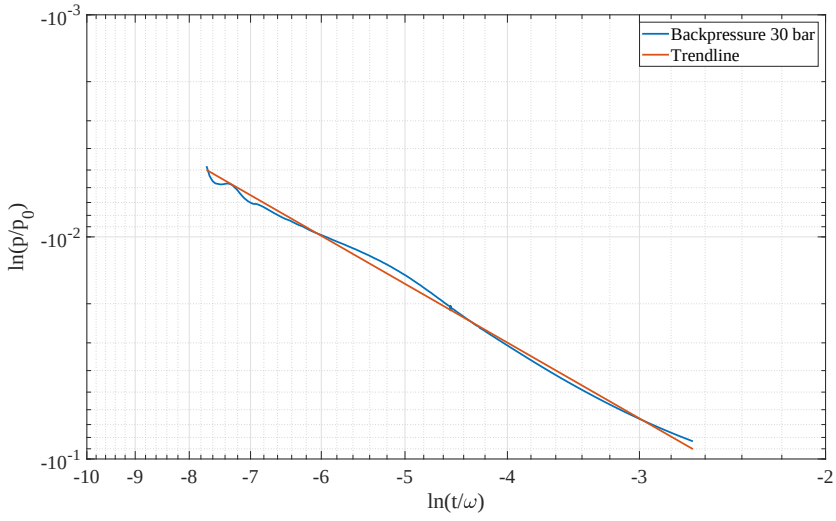

Figure B.26: Dimensionless plot for outlet area 12.56 mm^2 backpressure 30.7 bar, with pre-charge setting 1.

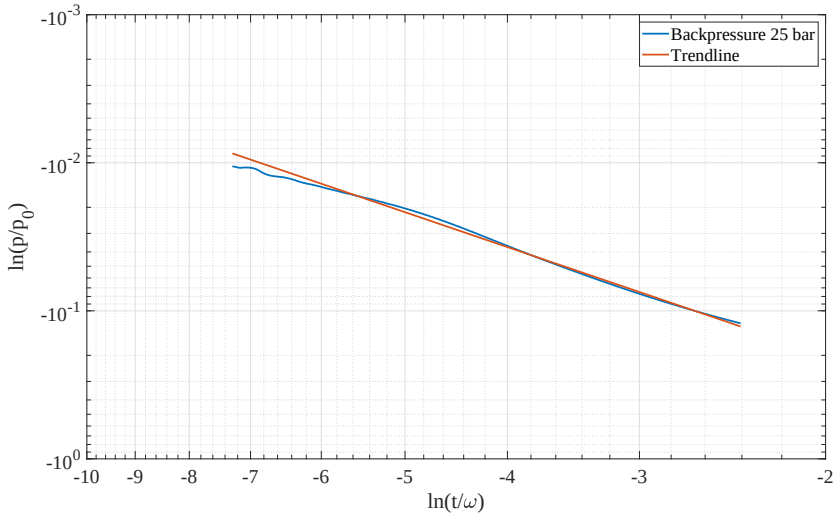

Figure B.27: Dimensionless plot for outlet area 12.56 mm^2 backpressure 25 bar, with pre-charge setting 1.

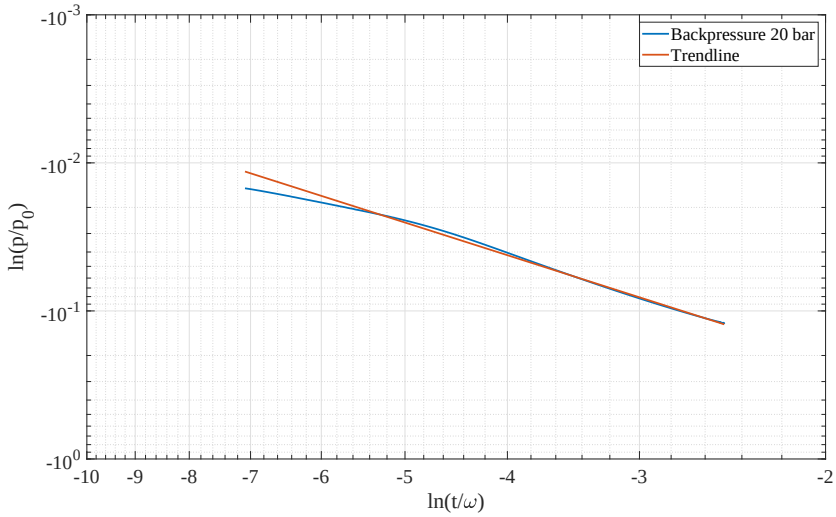

Figure B.28: Dimensionless plot for outlet area 12.56 mm^2 backpressure 20 bar, with pre-charge setting 1.

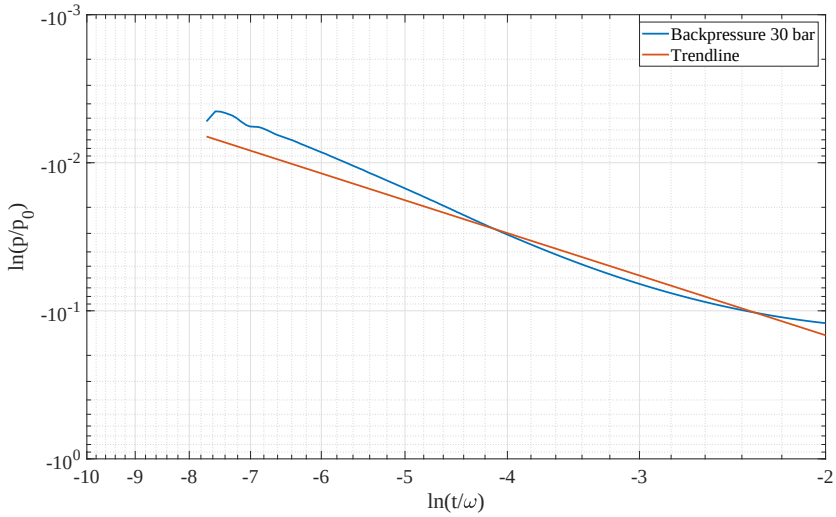

Figure B.29: Dimensionless plot for outlet area 12.56 mm^2 backpressure 30.7 bar, with pre-charge setting 2.

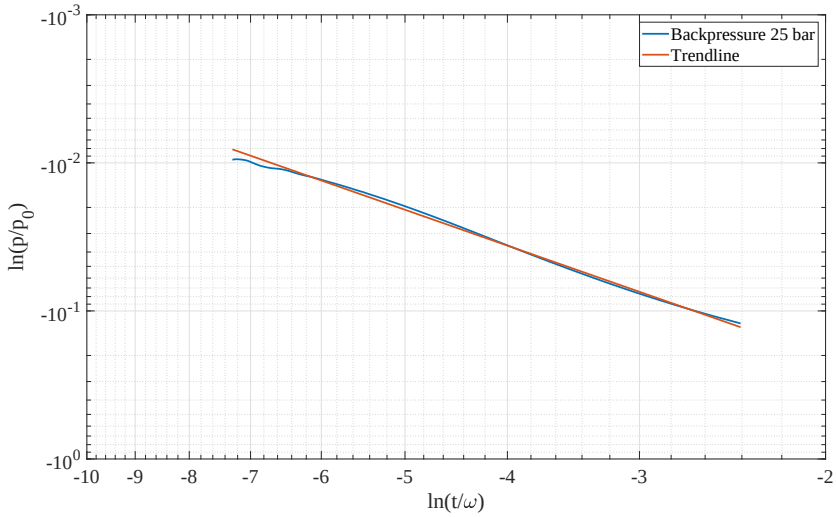

Figure B.30: Dimensionless plot for outlet area 12.56 mm^2 backpressure 25 bar, with pre-charge setting 2.

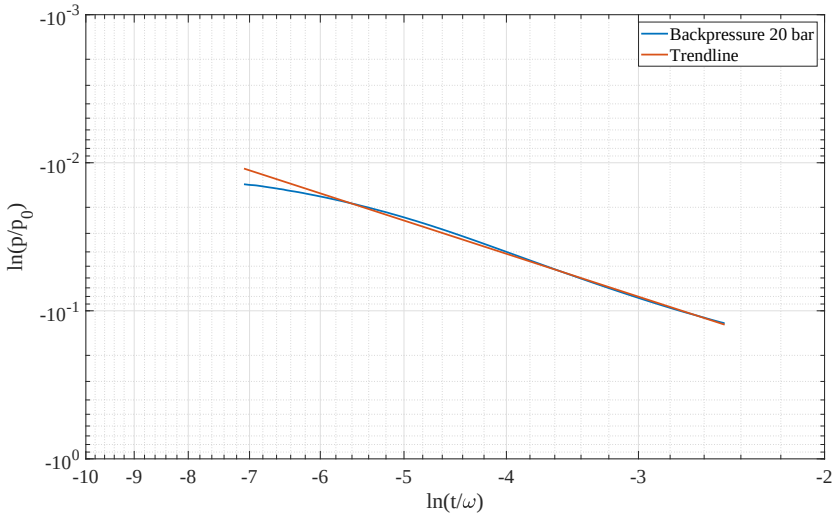

Figure B.31: Dimensionless plot for outlet area 12.56 mm^2 backpressure 20 bar, with pre-charge setting 2.